Vortex-induced Rings and Gaps in Protoplanetary Disks

by

Xiaoyi Ma
B.Sc., University of Toronto, 2021

A Thesis Submitted in Partial Fulfillment of the
Requirements for the Degree of

MASTER OF SCIENCE

in the Department of Physics and Astronomy

Vortex-induced Rings and Gaps in Protoplanetary Disks

by

Xiaoyi Ma
B.Sc., University of Toronto, 2021

Supervisory Committee

Dr. Ruobing Dong, Supervisor
(Department of Physics and Astronomy)

Dr. Doug Johnstone, Departmental Member
(Department of Physics and Astronomy)

ABSTRACT

Observations of protoplanetary disks have revealed both crescents and rings in dust continuum emission. These crescents are believed to result from dust-trapping vortices generated by the Rossby Wave Instability (RWI), which induces density waves similar to those produced by planets. We explore the properties of these density waves and associated substructures by performing 2D hydrodynamic simulations both in shearing boxes and global disks. Our findings confirm that long-lived vortices can indeed create observable rings and gaps in inviscid discs consistent with ALMA dust continuum observations. Additionally, we establish an empirical relationship between the aspect ratio of gas vortices and the location of dust rings, revealing a linear correlation between them.

Contents

List of Tables

List of Figures

ACKNOWLEDGEMENTS

I would like to thank:

Ruobing Dong and Pinghui Huang for mentoring, support, encouragement, and patience.

My family, my cats and my friends, for supporting me in the low moments.

Cong Yu, Doug Johnstone, Jeffrey Fung, Josh Calcino, Gianluigi Bodo,

Haochang Jiang, Kengo Tomida, Rixin Li and Tomohiro Ono, for insightful suggestions and discussions.

DEDICATION

To my cherished family, supervisor, mentors, dear friends, and all those who crossed my path. Your support has illuminated my journey.

Chapter 1

Introduction

1.1 Protoplantary Disk

In the vast expanse of the cosmos, planets emerge from the cosmic dust and gas, with one, in particular, evolving into our cherished home. In recent years, significant advancements in exoplanet detection have unveiled over five thousand distant worlds outside of our solar systems. However, despite their prevalence, the formation of these planets remains one of the most intriguing puzzles in the field of astronomy.

Planets are thought to originate within protoplanetary disks, which are rotating disks of gas and dust that surround newly formed stars. The most direct approach to studying planet formation is by observing this process in action — specifically, by searching for young planets at various stages of formation. However, directly observing protoplanets is challenging because planets are much dimmer than both the disk and the star. As a result, only a few protoplanets have been detected by direct imaging, such as PDS 70 b [Keppler et al., 2018], PDS 70 c [Haffert et al., 2019], AB Aurigae b [Currie et al., 2022] and HD 169142 b [Hammond et al., 2023].

Apart from direct imaging of protoplanets, we can also learn about planet formation from disk morphologies. The formation of planets is influenced by their interactions with material within the protoplanetary disk, where the process is more likely to be initiated in regions of higher density. Consequently, the signatures of the planet formation process are imprinted on the structures of the disks. By investigating and observing these disk structures, we can gain valuable insights into the process of planet formation.

Recent high-resolution observations of both scattered light and dust continuum emissions have revealed that structures such as rings and gaps are commonly found within protoplanetary disks [Andrews et al., 2018, Long et al., 2018]. Rings, believed to correspond to variations in dust density, where dust accumulates within local pressure maxima, may play a critical role in planet formation. They facilitate the growth of dust particles to larger sizes and prevent them from drifting inward. Given our current limited understanding of the planet formation, investigating the impact of these dust traps could be essential for advancing our comprehension of this complex process.

1.2 Previous work

Although rings may play an important role in understanding the physics of both disk evolution and planet formation, their origins remain unclear. There are a variety of hypothesized mechanisms proposed to explain the formation of rings within protoplanetary disks. These mechanisms can be categorized into the following three types: fluid mechanics, dynamical interactions with companions, and condensation fronts [Andrews, 2020].

The disk is subject to various turbulent motions and instabilities that can perturb its density distribution and produce rings. In young disks, disk winds driven by magnetorotational instability (MRI) can remove material from the inner disk, creating an inner cavity. Dust particles are expected to concentrate at the edge of this cavity, resulting in a ring-like structure known as a ring-hole [Takahashi and Muto, 2018].

The magnetorotational instability can also induce zonal flows, which are created by variations in the orbital velocity, similar to the latitudinal flows in planetary atmospheres. They may lead to long-lived axisymmetric pressure variations due to geostrophic balance [Armitage, 2017]. These variations can reduce the radial drift of dust grains and concentrate them into pressure bumps, ultimately forming dust rings [Johansen et al., 2009].

Additionally, in non-ideal magneto-hydrodynamics (MHD), ambipolar diffusion (AD) may steepen the midplane current sheet into thin layers, resulting in a highly pinched poloidal magnetic field within these layers. Reconnection of this pinched field generates detached magnetic loops in the local disk with reduced magnetic flux. As mass accretion is driven by the removal of angular momentum due to the Lorentz force, which is related to magnetic flux, the reconnection of the poloidal field leads to slow accretion and the formation of rings.[Suriano et al., 2018].

When the dust-to-gas ratio reaches order unity, the gas-dust coupling can also lead to the formation of rings within the disk. Specifically, when the dust-to-gas ratio is increased and turbulence is minimal, the combination of gas-dust coupling and the self-gravity of both dust and gas can trigger secular gravitational instability [Takahashi and Inutsuka, 2014]. This process shears over-densities into narrow rings within the disk [Andrews, 2020].

Rings can also form within the disk without pressure bumps, but rather at condensation lines [Zhang et al., 2015]. This mechanism involves two main components. Firstly, the presence of ice significantly affects the critical velocity for fragmentation. This velocity can decrease across the snowline, leading to destructive collisions and the formation of smaller dust grains inside of the snowline. These smaller dust grains, well-coupled with gas, experience significantly slower radial drift velocities compared to icy pebbles outside the snowline, resulting in a "traffic jam" effect and the accumulation of dust particles inside the snowline. Secondly, water vapour liberated from icy pebbles could be recycled back outside of the snowline and recondensed, leading to the piling up of icy pebbles outside of the snowline [Birnstiel et al., 2010, Drażkowska and Alibert, 2017]. Evidence of fast pebble growth near the condensation fronts has been found in observations, where the expected condensation fronts of main volatiles, determined by the midplane temperature distribution derived from observation, coincide with emission dips in the dust continuum [Zhang et al., 2015].

Rings can also be produced by interactions with companions. One of the most common and well-studied explanations for ring-like structures is planet-disk interaction. The gravitational perturbation induced by a planet can generate density waves at Lindblad resonance. The angular momentum carried by the wave is transferred to the local disk through shock dissipation, thereby moving material from the planetary orbit and resulting in the formation of gaps. Dust accumulates at the pressure maxima outside of these gaps, resulting in the formation of dust rings [Lin and Papaloizou, 1986].

There is also a possibility that the rings we observed are caused by irradiation instability in a passively heated disk, rather than actual overdensities of dust [Kutra et al., 2024]. In this work, we only focus on the dust ring produced by actual dust overdensities.

1.3 This work

In this study, we introduce a novel mechanism for producing rings and gaps within protoplanetary disks through vortex-induced density waves. This innovative approach is inspired by the fact that vortices generate density waves similar to those induced by planets [Paardekooper et al., 2010], and such vortices have been observed in several disks as dust-trapping crescents [van der Marel et al., 2020]. For this work, our aim is to begin investigating this new mechanism by exploring the interaction between a long-lived vortex and a disk in inviscid environment.

The key findings of our work include:

- Through hydrodynamic simulations in a shearing box and analysis of vortex-induced density waves, we confirm the ability of vortex-induced waves to transport angular momentum through shock dissipation and redistribute disk materials, leading to the formation of dust rings in an inviscid disk.
- Utilizing radiative transfer simulations, we generate synthetic images of global simulations that closely resemble real observations. This confirms the detectability of vortex-induced rings in ALMA observations.
- We establish an empirical relationship between the aspect ratio of the gaseous vortex and the location of the dust ring, derived from simulations of different disk models producing vortices with varying strengths.

These findings collectively present a novel mechanism for producing rings and gaps within inviscid disks via long-lived vortices, offering a new avenue for structure formation within disks.

1.4 Overview

The thesis is organized as follows:

Chapter 2 introduces the specific problems we have addressed in this study.

Chapter 3 presents the methodologies and algorithms employed in our research.

Chapter 4 presents the simulation results.

Chapter 5 explores the properties of vortices within the disk and their correlation with the resulting structures. This chapter also includes a comparison between synthetic images from global simulations and real observations, along with a discussion on the feasibility of vortex-disk interaction in producing observable rings within a realistic disk environment.

Chapter 6 summarizes our findings and conclusions, with additional details provided in the appendix.

Chapter 2

The Problem to be Solved

In recent decades, high-resolution observations have unveiled the presence of substructures, such as rings and gaps, within protoplanetary disks. These rings, which exhibit azimuthal symmetric denser regions, are significant sites for the formation of planetesimals — kilometre-sized bodies formed in the process of planet formation. Understanding the formation processes of these substructures is crucial for comprehending disk evolution and planetary formation.

One prominent explanation for the formation of such substructures is the gravitational interaction between already-formed young planets and protoplanetary disks. This interaction triggers constructive density waves at Lindblad resonance. As these density waves propagate and undergo shock, they transfer angular momentum to the disk material, potentially leading to the formation of gaps and rings within the disks [Dong et al., 2011b]. Consequently, these rings and gaps are regarded as signspots of hidden embedded protoplanets within the disks and at specific distances from the rings.

However, detecting these embedded planets is significantly challenging due to their dimness compared to the brightness of the disk and the central star. Only very few protoplanet candidates have been detected in the disks by direct imaging out of the hundreds of disks exhibiting rings and gaps. Consequently, observed rings and gaps in the majority of disks without confirmed planet detection are possibly attributed to other mechanisms rather than planet-disk interaction.

In addition, dust rings and gaps have been found in disks so young that the local material has only had time to finish on the order of 1,000 orbits [Segura-Cox et al., 2020]. Whether planets can form and generate disk structures so quickly remains unclear.

Moreover, the rings themselves serve as prime locations for planet formation, leading to a chicken-and-egg situation where a planet is required to produce structures that facilitate its own formation. To fully understand the disk-planet interaction mechanism, additional explanations of planetary formation within these disks are necessary, but such explanations are currently inconclusive. It is more likely that the initial rings in the disk are formed by mechanisms that do not require the presence of a planet.

Therefore, we aim to find an alternative mechanism for generating rings and gaps within protoplanetary disks, without requiring a planet: large-scale vortices. Theoretically, these gaseous vortices can persist for long periods and efficiently trap dust particles within their asymmetric pressure maxima, manifesting as dust-trapping crescents in continuum emission. Observations have revealed the coexistence of crescents and rings in several protoplanetary disks [Andrews et al., 2018].

Vortices within the disk have been proposed to form via the Rossby Wave instability (RWI) [Lovelace and Hohlfeld, 1978, Lovelace et al., 1999, Li et al., 2000]. A sharp radial variation in density, resulting in a steep radial gradient in gas density, can trap local Rossby waves and trigger RWI in low-turbulent discs. This process leads to the production of large-scale vortices at a nonlinear stage. RWI can be triggered by density variations at the cavity outer edge of the transitional disk or planet-induced gaps [Lin and Papaloizou, 1986, Zhu et al., 2014]. It also can operate on rings with a width comparable to or less than the disk scale height, or on a pressure bump. They can also be produced due to a sharp viscosity change at the edge of dead zones [Li and Li, 2015, Miranda et al., 2017], where MRI is suppressed by non-ideal MHD effects [Bai and Stone, 2014].

In our work, we trigger the RWI by introducing a Gaussian pressure bump into the background density wave profile. This method generates vortices akin to those produced by other mechanisms. We adopt this approach as it allows us to isolate the interaction between the vortex and the disk from other factors affecting the disk, such as viscosity variation near the dead zone and density waves induced by planets. In general, our emphasis is on studying the subsequent evolution of vortex-disk interaction rather than the vortex-formation process.

The RWI vortex we consider is a large-scale compressible anticyclonic vortex, where the gas fluid and streamlines revolve around the center of the vortex. This type of vortex can be characterized by several factors, including its distance from the system center, gas density at the vortex center, and its size and shape (e.g., aspect ratio), which determine the turnover time and migration timescale of the vortex.

Can these RWI vortices generate observable rings and gaps within disks? The first step to address this question is to explore the interaction between the long-lived vortex and disks, particularly within an inviscid environment. Theoretically, the motion of these vortices induces velocity perturbations, exciting density waves in the disk, analogous to planet-induced density waves [Paardekooper et al., 2010]. Consequently, vortex-induced density waves also have the potential to transfer angular momentum carried by them to the local disk material, thereby creating rings and gaps. However, to assess the feasibility of vortex-disk interaction in generating observable features in real disks, various factors including viscosity, vortex formation, vortex longevity, and ring lifetime need to be taken into account, which fall beyond the scope of the present study.

This project aims to verify whether a long-lived RWI vortex can indeed induce rings and gaps in inviscid discs. To achieve our goal, we investigate the properties of density waves induced by RWI vortices using hydrodynamic simulations. We then examine the substructures produced by these density waves. Subsequently, we validate our findings by comparing our simulation results with observations using radiative transfer modeling.

Chapter 3

Method

The primary goal of our work is to investigate whether long-lived vortices have the ability to generate rings and gaps within inviscid discs. To achieve this goal, we induce a Gaussian pressure bump to the background density and carry out hydrodynamical simulations within the shearing box, to avoid complications associated with vortex migration. Additionally, we perform simulations in the global disk to compare with observations. These simulations are conducted using the grid-based hydrodynamical simulation code Athena++ [Stone et al., 2020] to solve the Navier-Stokes equations as described in the section 3.1 below.

3.1 Navier-Stokes Equations

3.1.1 Shearing box

In the shearing box approximation, we consider barotropic and purely hydrodynamic disks orbiting around a central star in a 2D local co-moving Cartesian coordinate. We neglect the effects of viscosity, self-gravity, dust feedback, dust diffusion and magnetic field.

The shearing box approximation adopts a frame of reference at the radius r_0 co-rotating with the disk at the orbital velocity $\Omega_0 = \Omega(r_0)$. In this frame, the 2D hydrodynamics equations are written in a Cartesian coordinate system (x, y, z) that has the unit vector $\hat{\mathbf{i}}$, $\hat{\mathbf{j}}$ and $\hat{\mathbf{k}}$ as [Stone and Gardiner, 2010]:

$$\begin{aligned} \frac{\partial \Sigma_{\mathrm{g}}}{\partial t} + \nabla \cdot [\Sigma_{\mathrm{g}} \mathbf{v}_{\mathrm{g}}] &= 0 & (3.1) \\ \frac{\partial \Sigma_{\mathrm{g}} \mathbf{v}_{\mathrm{g}}}{\partial t} + \nabla \cdot [\Sigma_{\mathrm{g}} \mathbf{v}_{\mathrm{g}} \mathbf{v}_{\mathrm{g}} + P] &= \Sigma_{\mathrm{g}} \Omega_0^2 (2qx\hat{\mathbf{i}}) - 2\Omega_0 \hat{\mathbf{k}} \times \Sigma_{\mathrm{g}} \mathbf{v}_{\mathrm{g}} & (3.2) \end{aligned}$$

The above equations 3.1 to 3.2 are the gas continuity and momentum equations, respectively, where Σ_{d} is the gas surface density, $\mathbf{v}_{\mathrm{g}}$ is the gas velocity and P is the gas pressure. We assume an isothermal disk, in which case $P = c_s^2 \Sigma_{\mathrm{g}}$, where c_s is the constant isothermal sound speed. In the code unit, c_s equals 0.1. The shear parameter q is defined as

$$q = -\frac{1}{2} \frac{d \ln \Omega^2}{d \ln r} \tag{3.3}$$

For Keplerian flow, $q = 3/2$. In this work, we included a dust fluid module in Athena++ [Huang and Bai, 2022] by treating dust as pressureless fluid. The continuity and momentum equations for dust are defined as follows:

$$\begin{aligned} \frac{\partial \Sigma_{\mathrm{d}}}{\partial t} + \nabla \cdot [\Sigma_{\mathrm{d}} \mathbf{v}_{\mathrm{d}}] &= 0 & (3.4) \\ \frac{\partial \Sigma_{\mathrm{d}} \mathbf{v}_{\mathrm{d}}}{\partial t} + \nabla \cdot [\Sigma_{\mathrm{d}} \mathbf{v}_{\mathrm{d}} \mathbf{v}_{\mathrm{d}}] &= \Sigma_{\mathrm{d}} \Omega_0^2 (2qx\hat{\mathbf{i}}) - 2\Omega_0 \hat{\mathbf{k}} \times \Sigma_{\mathrm{d}} \mathbf{v}_{\mathrm{d}} + \Sigma_{\mathrm{d}} \frac{\mathbf{v}_{\mathrm{g}} - \mathbf{v}_{\mathrm{d}}}{t_s} & (3.5) \end{aligned}$$

The symbols are defined similarly to the gas fluid. The stopping time, t_s, represents the timescale over which the velocity of dust particles exponentially decays due to aerodynamic drag. For our simulation, we only consider one dust species, ignoring dust diffusion. We also do not include dust feedback, which involves the drag exerted by dust on the gas flow when the dust-to-gas ratio reaches or exceeds unity.

In our work, we employ the grid-based hydrodynamical simulation code Athena++ [Stone et al., 2020] to solve the equations outlined above. We utilize the second-order piecewise linear spatial reconstruction method (PLM) to obtain solutions. To reduce computational costs, we incorporate the orbital advection algorithm, initially introduced in the FARGO code [Masset, 2000] and later implemented into Athena [Stone et al., 2020]. This algorithm decomposes the velocity field into steady background orbital motion and velocity fluctuations, allowing us to solve the equations separately for the linear orbital advection part and typical hydrodynamical equations. Consequently, the computational time step depends solely on the amplitude of velocity fluctuations, thereby increasing the length of the time step and reducing computational costs.

3.1.2 Global disks

In global simulations, we consider a locally isothermal and weakly viscous disk orbiting around a central star. Similarly, to the simulations for shearing box approximation, we utilize Athena++ [Stone and Gardiner, 2010] to solve the equations for continuity and momentum within the global disk. These equations are expressed in a polar coordinate system (r,ϕ) [Huang and Bai, 2022]:

$$\begin{aligned}
\frac{\partial \Sigma_{\mathrm{g}}}{\partial t} + \nabla \cdot [\Sigma_{\mathrm{g}} \mathbf{v}_{\mathrm{g}}] &= 0 && (3.6)\\
\frac{\partial \Sigma_{\mathrm{g}} \mathbf{v}_{\mathrm{g}}}{\partial t} + \nabla \cdot [\Sigma_{\mathrm{g}} \mathbf{v}_{\mathrm{g}} \mathbf{v}_{\mathrm{g}} + P] &= -\Sigma_{\mathrm{g}} \nabla \Phi_* - \nabla \cdot \Pi_\nu && (3.7)\\
\frac{\partial \Sigma_{\mathrm{d}}}{\partial t} + \nabla \cdot [\Sigma_{\mathrm{d}} \mathbf{v}_{\mathrm{d}} + \Sigma_{\mathrm{d}} \mathbf{v}_{\mathbf{d},\mathrm{dif}}] &= 0 && (3.8)\\
\frac{\partial \Sigma_{\mathrm{d}} (\mathbf{v}_{\mathrm{d}} + \mathbf{v}_{\mathbf{d},\mathrm{dif}})}{\partial t} + \nabla \cdot [\Sigma_{\mathrm{d}} \mathbf{v}_{\mathrm{d}} \mathbf{v}_{\mathrm{d}} + \Pi_{\mathrm{dif}}] &= -\Sigma_{\mathrm{d}} \nabla \Phi_* + \Sigma_{\mathrm{d}} \frac{\mathbf{v}_{\mathrm{g}} - \mathbf{v}_{\mathrm{d}}}{t_s} && (3.9)
\end{aligned}$$

The symbols are defined similarly to the shearing box approximation. Φ_* is the stellar gravitational potential, which is equal to GM_*/r. Here, G denotes the gravitational constant, M_* represents the mass of the star, and r represents the distance from the star. In the code unit, GM_* is equal to 1. The viscous stress tensor Π_ν is given by:

$$\Pi_{\nu,ij} = -\Sigma_{\mathrm{g}} \nu \left(\frac{\partial v_{\mathrm{g},i}}{\partial x_j} + \frac{\partial v_{\mathrm{g},j}}{\partial x_i} - \frac{2}{3} \frac{\partial v_{\mathrm{g},k}}{\partial x_k} \delta_{ij} \right) \qquad (3.10)$$

where $\nu = \alpha c_s h$ is the coefficient kinematic viscosity. h is the disk scale height and α denotes the Shakura-Sunyaev viscosity parameter [Shakura and Sunyaev, 1973]. In the global disk simulation, α is equal to 10^{-5}.

In global disk simulations, we incorporate dust diffusion due to the stirring of particles by turbulent gas [Youdin and Lithwick, 2007], which is characterized by the effective dust drift speed $\mathbf{v}_{\mathbf{d},\mathrm{dif}}$ resulting from concentration diffusion. The corresponding momentum diffusion flux tensor is given by:

$$\Pi_{\mathrm{dif},ij} = \Sigma_{\mathrm{d}} \left(v_{\mathrm{d},j} v_{\mathrm{d,dif},i} + v_{\mathrm{d},i} v_{\mathrm{d,dif},j} \right) \qquad (3.11)$$

Similar to simulations for the shearing box approximation, we utilize the second-order piecewise linear spatial reconstruction method (PLM) to obtain solutions along with orbital advection.

3.2 Initial and Boundary Conditions

3.2.1 Shearing box

We perform the simulations on various initial conditions to investigate vortex properties and the characteristics of the corresponding substructures. The initial conditions are summarized in the Table 3.1 below.

Name	$\Delta w_0/h$	A_0	m_*	lx	ly
A1	0.632	0.439	4	$\{-20h, 20h\}$	$\{-8h, 8h\}$
A2	0.632	0.358	4	$\{-20h, 20h\}$	$\{-8h, 8h\}$
A3	0.632	0.227	3	$\{-30h, 30h\}$	$\{-10.5h, 10.5h\}$
A4	0.632	0.205	3	$\{-30h, 30h\}$	$\{-10.5h, 10.5h\}$

Table 3.1: Parameters for Disk Models. The first three parameters are adopted from Table 1 in [Ono et al., 2018]. A_0 is the amplitude of the pressure bump, and $\Delta w_0/h$ is the width of the pressure bump in the unit of disk scale height h. In the shearing box, $h = 0.1$. m_* is the most unstable azimuthal mode of RWI. lx and ly is the simulation domain for each model.

To trigger the formation of vortices via Rossby Wave Instability, we initialize the gas density with a Gaussian bump peaked at $x = 0$ on a uniform profile [Ono et al., 2018]:

$$\Sigma_\mathrm{g}(x, y) = \Sigma_{\mathrm{g},n}\left(1 + A_0 e^{-\frac{1}{2}\left(\frac{x-x_0}{\Delta w_0}\right)^2}\right) \tag{3.12}$$

where $\Sigma_{\mathrm{g},n}$ is the background density profile, and the density is uniform along y direction. For our simulations in the shearing box, we set $\Sigma_{\mathrm{g},n} = 1$. A_0 represents the amplitude of the bump, and Δw_0 denotes the radial half-width of the bump, which is equal to 0.632 h in our simulation. In the code unit, Ω equal 1 and c_s equals 0.1, hence the disk scale height $h = c_s/\Omega = 0.1$. x_0 represents the location of the bump, which is equal to 0 in our simulations. We vary the amplitude of the bump A_0 to generate vortices with different strengths.

For barotropic disks, the gas pressure is a function of the density only, so the gas pressure is initialized as $P = c_s^2 \Sigma_\mathrm{g}$.

Table 3.1 presents four disk models utilized as initial conditions for gas density. In these models, m_* denotes the most unstable azimuthal mode of RWI adopted from

[Ono et al., 2018]. They are calculated analytically in a linear regime of RWI as described in [Ono et al., 2016], indicating the number of vortices triggered at the beginning of the simulation before RWI saturated [Ono et al., 2018].

The grid is uniformly spaced within the simulation domains. Each model has different simulation domains in the y direction based on their most unstable azimuthal mode. To avoid complications associated with vortex merging, we truncate the full azimuthal domain in the y direction based on the number of primary vortices indicated by their most unstable azimuthal mode. Therefore, we include only one of the primary vortices within the simulation domain when RWI is initially triggered and throughout the full simulation. The simulation domains in the x direction are set according to the strength of the vortex. A lower bump triggers a weaker vortex, which induces a density wave shocked further away from the vortex [Paardekooper et al., 2010]. Hence, we extend the simulation domain in the x direction for weaker vortices to fully capture the shock dissipation of their density wave.

Since our goal is to investigate substructures resulting from shock dissipation of vortex-induced density waves, it is crucial for our simulations to have sufficient resolution to probe the evolution of the density waves. This ensures that the shock locations of density waves and density profiles reach convergence with resolutions, therefore the impact of numerical diffusion is negligible. Following the convergence test outlined in appendix A, we determine that a resolution of 256 cells/h is appropriate for our simulations.

The initial gas velocities are set by hydrostatic equilibrium. In addition, we impose a small initial gas velocity perturbation in x direction according to the most unstable azimuthal mode in Table 3.1 to trigger the RWI :

$$v_{\mathrm{g,x}} = 10^{-5}\cos{(m_* y)}e^{-\frac{1}{2}(\frac{x}{0.1})^2} \tag{3.13}$$

$$v_{\mathrm{g,y}} = -q\Omega_0 x + \frac{1}{2\Omega\Sigma_g}\frac{\mathrm{d}P}{\mathrm{d}x} \tag{3.14}$$

In our simulations, we consider only one dust species with a Stokes number given by $St = t_s\Omega_k = 0.1$. Ω_k is the Keplerian angular speed that defined as $\sqrt{GM_*/r^3}$. The initial dust density follows the gas density described by Equation 3.12 with a uniform dust-to-gas ratio of 0.01. The initial dust velocities are also set to hydrostatic equilibrium.

The boundary condition is periodic in the x direction and shearing periodic in the y direction. To minimize the reflecting wave along x edges, we add a wave-damping zone along the x boundaries with a damping rate $\zeta_{\rm dr} = 100$ and damping ratio $\epsilon = 1.2$. The damping zone is defined as $\{\epsilon^{-2/3}x_{\max}, x_{\max}\}$ and $\{x_{\min}, \epsilon^{-2/3}x_{\min}\}$, which $x_{\min}$ is the inner edge of the x domain and $x_{\max}$ is the outer edge. In the outer damping zone, all variables will gradually be damped to the initial values by the following equation [Huang and Bai, 2022]:

$$\frac{\partial X}{\partial t} = \zeta_{\rm dr}\Omega_0(X_0 - X)\left(\frac{x - \epsilon^{-2/3}x_{\max}}{x_{\max} - \epsilon^{-2/3}x_{\max}}\right)^2 \tag{3.15}$$

where X_0 is the initial value and X represents gas density, dust density and velocities. Similarly, the equation for damping at the inner edge is obtained by replacing $x_{\max}$ with $x_{\min}$.

3.2.2 Global disks

Our analysis primarily relies on simulations conducted within the shearing box framework. However, we also conduct global simulations to compare with real observations. Due to the limitation of computational resources, we only run global simulations for the 'A2' disk model listed in Table 3.1. This model features a relatively strong vortex that rapidly forms the dust ring.

In the global disk simulations, we applied the same pressure bump as defined in Equation 3.12, using the model parameters for 'A2' listed in table 3.1, at the initial location of the vortex at $r = 1.5$. Additionally, we modified the background density profile to follow a power law, expressed as $\Sigma_{\rm g,n} = \Sigma_{\rm g,0}(r/r_0)^{-n}$, where r_0 represents a reference radius set to 1.0. The density gradient n was set to 0.5 in the simulations. We assume the disk is locally isothermal in the global simulation, $P = c_s^2\Sigma_{\rm g}$, in which the sound speed profile is described as $c_s = c_{s,0}(r/r_0)^{-1/4}$, where $c_{s,0} = 0.1$. We would like to mention that locally isothermal simulations have a tendency to overestimate the density contrast of the rings and gaps. This is primarily due to the nonconservation of the angular momentum flux, where the wave exchange angular momentum with the locally isothermal disk as they propagate [Miranda and Rafikov, 2019].

Our simulation domain covers a radial range of $r \in [0.1, 3.2]$ spaced as a geometric sequence with a common ratio of 1.01 and uniformly extends over the full azimuthal range of $\phi \in [0, 2\pi]$.

The simulation runs on a root mesh grid of $N_r \times N_\phi = 62 \times 192$. We apply the static mesh refinement at level 4 for $r \in [0.25, 2.5]$ near the vortex to probe the evolution of density waves. Each level of refinement doubles the resolution, so the resolution in the radial direction at $r = 1$ reaches 33 cells/h after the mesh refinement.

For global disks, the initial velocities are set by hydrostatic equilibrium for both dust and gas. We add small velocity perturbations in white noise with an amplitude of $0.01c_s$ in both radial and azimuthal directions to trigger the instability.

Similar to simulations in the shearing box, we consider only one dust species with a Stokes number given by $St = 0.1$. The initial dust density follows the gas density with a uniform dust-to-gas ratio of 0.01. To prevent the rapid inward drift of dust particles towards the inner boundary at the beginning of the simulation, we initiate dust motion at $t = 200$ orbits.

Periodic boundary conditions are applied along ϕ directions. The radial boundary condition is fixed by the initial values. In addition, a damping zone described in Equation 3.15 is added along the radial boundary, with damping rate $\zeta_{\mathrm{dr}} = 1$ and a damping ratio as $\epsilon = 1.2$, which results in an inner damping zone of $r \in [0.100, 0.113]$ and an outer damping zone of $r \in [2.834, 3.200]$.

3.3 Metrics

To study the vortex-induced substructures, we aim to extract several properties from the simulations in the shearing box. Below, we outline the metrics that characterize the simulation properties of interest.

3.3.1 Vortex structure

In a shearing box setup, the vortex center is positioned at the origin of the frame. At the vortex center, the radial gas velocity reaches zero, which $v_{\mathrm{g},x}(0, 0) = 0$. Similarly, the azimuthal gas velocity perturbation $\delta v_{\mathrm{g},y} = v_{\mathrm{g},y} - v_k$ also reaches zero at the vortex center, where v_k represents the background Keplerian velocity [Ono et al., 2018].

These velocity profiles from the simulations also depict the vortex core. In the vicinity of the vortex, both $v_{\mathrm{g},x}(0, y)$ cutting through the vortex center along y direction and $\delta v_{\mathrm{g},y}(x, 0)$ cutting through the vortex center along x direction varies according to the distance from the vortex center, reaching their local extremes and falling back to zero as moving further away from the vortex. The velocity profiles reach their extremes approximately at the edge of the vortex core [Fung and Ono, 2021].

Therefore, we define the size of the vortex based on its velocity profiles. The semi-major axis of the vortex core a_{v} is defined as half the distance between two extremes in $v_{\mathrm{g,x}}$, and the semi-minor axis of the vortex core b_{v} is defined as half the distance between two extremes in $\delta v_{\mathrm{g,y}}$, as shown in Figure 5.1. Hence, the aspect ratio of the gaseous vortex is defined as $\chi_{\mathrm{v}} = a_{\mathrm{v}}/b_{\mathrm{v}}$.

The shape (aspect ratio) and size of the vortex serve to characterize the strength of the vortex, which allows us to determine its turnover time and velocity gradient using an analytic vortex solution, as well as its migration timescale in the global disk [Ono et al., 2018].

3.3.2 Shock location indicator

Since our goal is to investigate the structures generated by the shock dissipation of vortex-induced density waves, it is crucial to identify the shock location of the density wave.

For planet-induced density waves, the excitation and initial propagation of the density wave are not significantly affected by non-linearity for a planet with sufficiently low mass. Assuming a weakly nonlinear density wave, we can simplify the fluid equations to a single inviscid Burger's equation. With smooth density profiles as the initial condition, Burger's equation can be solved using the method of characteristics. When the characteristics of Burger's equation intersect, a double-valued solution is obtained, indicating the wave shocks. Hence, we can analytically calculate the shock location of the wave from Burger's equation under the assumption of weakly nonlinear waves [Goodman and Rafikov, 2001].

Unfortunately, determining the shock location analytically for vortex-induced density waves might be challenging due to the highly nonlinear nature of the RWI. Previous research on planet-disk interaction indicates that the shock wave disrupts the conservation of vortensity and angular momentum, resulting in the excitation of vortensity and the transfer of angular momentum carried by the wave to the local disk [Dong et al., 2011b]. Hence, we can estimate the shock location of the vortex-induced density waves by identifying peaks in vortensity and cutoffs in angular momentum flux. Here, we define the vortensity and angular momentum flux for simulations in the shearing box.

Vortensity (ζ) is also called potential vortensity and is defined as the following

[Cimerman and Rafikov, 2021]:

$$\zeta \equiv \frac{(\nabla \times \mathbf{v}_{\rm g})_z}{\Sigma_{\rm g}} \tag{3.16}$$

which is the z-component of vorticity $\omega = \nabla \times \mathbf{v}_{\rm g}$ divided by the surface gas density $\Sigma_{\rm g}$.

For a disk in a quasi-steady state, the time derivative of the perturbed angular momentum is zero, which is equal to the sum of angular momentum change due to mass accretion ($F_{\dot{M}}$), angular momentum flux carried by the wave (F_J) and torque for all external force (T) [Zhu et al., 2016]:

$$F_{\dot{M}}(x) + F_J(x) + T(x) = 0 \tag{3.17}$$

where the angular momentum flux carried by the wave is given by [Miranda and Rafikov, 2020]:

$$F_J(x) = \int_{y_{\rm min}}^{y_{\rm max}} \Sigma_{\rm g}(x,y)[v_{{\rm g},x}(x,y) - v_{{\rm g},x,0}(x,y)][v_{{\rm g},y}(x,y) - v_{{\rm g},y,0}(x,y)]\, dy \tag{3.18}$$

Before the wave shocks, angular momentum is conserved, and there is no mass accretion, so $F_J(x) = -T(x)$. All angular momentum generated by the torque of the vortex is carried away by the density waves. The angular momentum flux carried by the wave reaches a constant state in the vicinity of the vortex once the vortex reaches a quasi-steady state.

When the density wave shocks, it dissipates the angular momentum to the disk and drives accretion. The amount of angular momentum lost into the local disk is quantified as $-F_{\dot{M}}(x) = F_J(x) + T(x)$ [Zhu et al., 2016]. Since the total angular momentum is conversed, the angular momentum flux carried by the wave decreases $F_J(x) < -T(x)$ once the wave shocks. Therefore, the cut-offs in angular momentum flux carried by the wave indicate the shock location of the density waves.

3.4 Radiative Transfer and Synthetic Images

To compare with observations, the outputs of 2D hydrodynamic simulation in global disks are post-processed using the radiation transfer code RADMC-3D[1] [Dullemond

---

[1] https://www.ita.uni-heidelberg.de/ dullemond/software/radmc-3d/

et al., 2012] and the Common Astronomy Software Application (CASA)[2] [The CASA Team et al., 2022] to generate synthetic images for the dust continuum emission at 1.9 mm (ALMA band 4), following the procedure in a previous work [Huang et al., 2020].

As RADMC-3D reads 3D density distributions instead of surface densities, we convert the output 2D surface densities of gas and dust to 3D density distributions. Assume hydrostatic equilibrium for a vertically isothermal disk (the temperature of the gas is set by stellar irradiation), the 3D density distribution is given by [Armitage, 2020]:

$$\rho = \frac{1}{\sqrt{2\pi}} \frac{\Sigma(r, \phi)}{h(r)} e^{-z^2/2h(r)^2} \tag{3.19}$$

where ρ is the 3D density distribution, Σ denotes the surface density obtained from hydrodynamic simulations, and $h(r)$ signifies the disk scale height. The gas scale height is defined as $h_{\mathrm{g}}(r) \equiv c_s/\Omega$, We assume the dust scale height to be 10% of the gas scale height. Thereby, both the surface density of gas and dust can be converted to 3D density distributions using the provided equation.

We obtain the disk temperature from RADMC-3D using the stellar parameters of HD 135344B [Cazzoletti et al., 2018] under the assumption that the temperature is primarily influenced by sub-micron-sized dust particles. Given that such small dust particles are well-coupled with gas, we calculate the density of sub-micron-sized dust by scaling the gas density with a uniform dust-to-gas ratio of 0.01.

The dust opacity input for RADMC-3D is computed using optool [3] [Dominik et al., 2021], employing the DSHARP composition [Birnstiel et al., 2018] and a power-law dust size distribution given by $n(a) \propto a^{-3.5}$, where a represents the grain size. The minimum grain size considered is 0.1 μm, while the maximum grain size is set to 10 mm. Additionally, we assume that the dust grains are solid spheres without any porosity.

Subsequently, the dust emission is calculated using the ray-tracing method in RADMC-3D, incorporating the 3D dust density distribution computed by Equation 3.19 and the previously calculated disk temperature. In our computations, we also include the effect of dust scattering. As a result, we generate synthetic images without any noise.

To simulate the observation, we process the noise-free image from RADMC-3D

---

[2] https://casa.nrao.edu/

[3] https://github.com/cdominik/optool

using CASA to incorporate observational noise and convolve it with the appropriate beam size. We adopt the ALMA configuration of C4.8 similar to the real observation of HD 135344B [Cazzoletti et al., 2018], resulting a synthetic beam 0.079” × 0.070”. The synthetic image is produced with an integration time of 2 hours and thermal noise according to J. Pardo’s ATM model [Pardo et al., 2001].

Chapter 4

Result

We now present our main results from the simulations. Among the four disk models we simulated, listed in Table 3.1, we focus on model ‘A2’ ($A_0 = 0.358$) in this section. We chose this model for detailed analysis because it features a strong vortex capable of quickly opening up a gas gap, while also inducing shocks further away from the vortex. This allows us to distinguish between the impacts of vortex dynamics and shock dissipation on the disk.

4.1 Vortex-induced substructures

Figure 4.1 presents snapshots of the surface gas density and surface dust density, illustrating the evolution of the vortex and disk structures. The density bump undergoes RWI and generates a gaseous vortex at the center of the frame within tens of orbits, consistent with previous findings [Ono et al., 2018]. The vortex induces density waves in the gas, manifesting as spirals emerging from its tips. In later orbits, gas gaps form on each side of the vortex. Dust particles gradually accumulate inside the vortex or form dusty rings outside the gas gaps, resulting in a depletion of dust particles between the ring and the vortex, as well as outside the ring.

The time evolution of radial density profiles is depicted in Figure 4.2. As time progresses, the gas gap deepens, increasing the height of the pressure bump and the corresponding dust ring at the gap’s edge. Initially, we observe an inner ring forming at the inner edge of the pressure bump. However, as the pressure bump widens and the inner edge of the pressure bump moves closer to the vortex, the inner ring diminishes. By 450 orbits, the inner ring has vanished, as shown in Figure 4.1. Additionally, the

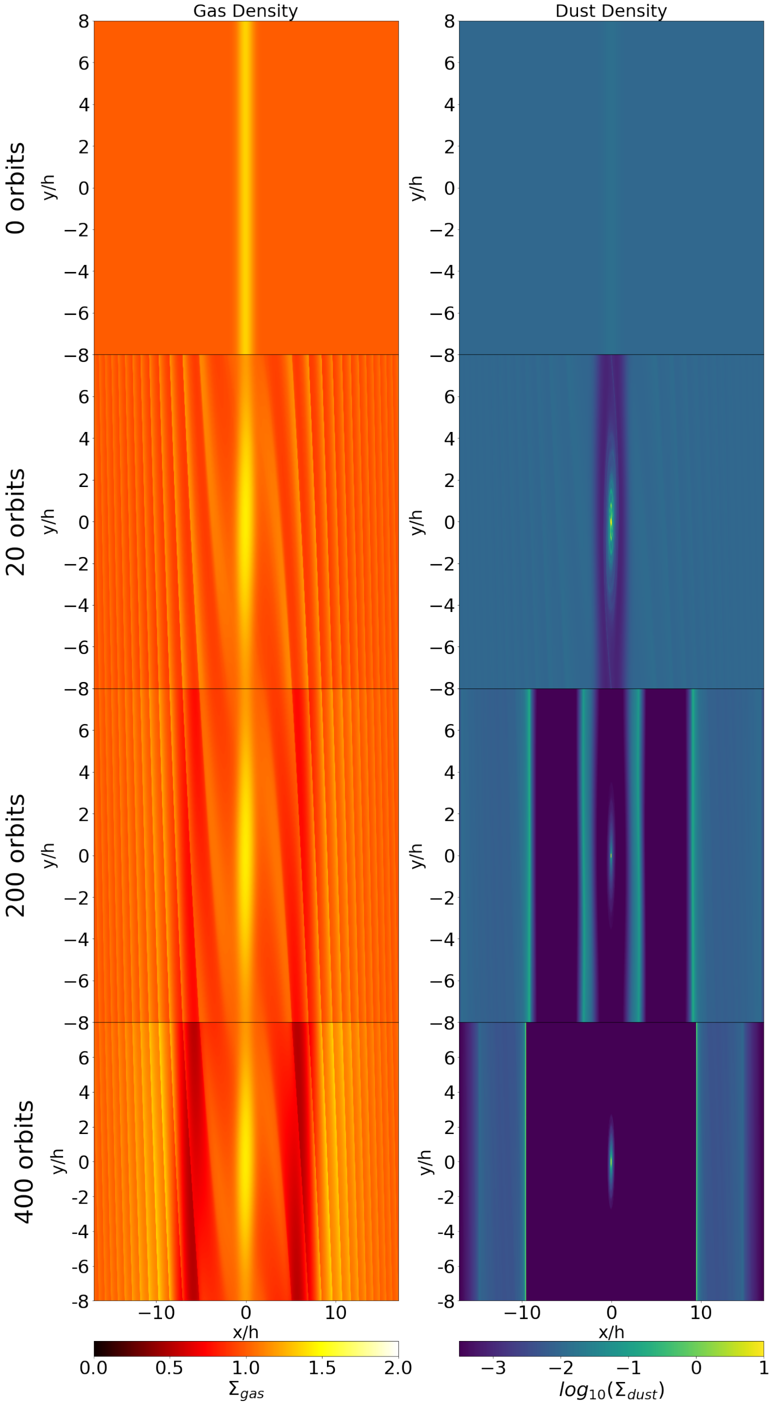

Figure 4.1: Surface density snapshots for dust and gas of model 'A2' ($A_0 = 0.358$), at different times (t = 0, 20, 200, and 400 orbits). The orbital period is defined as $2\pi\Omega_0^{-1} = 2\pi$. For an object orbiting around a solar mass star at a distance of 100 AU, it takes roughly 0.4 Myr to complete 400 orbits. The gas vortex formed at the center of the frame generates density waves as spirals coming from the tips of the vortex. At later orbits, gas gaps are produced on either side of the vortex. Dust grains are trapped within the vortex, and also in the pressure bump at the edge of the gas, thereby forming dusty rings.

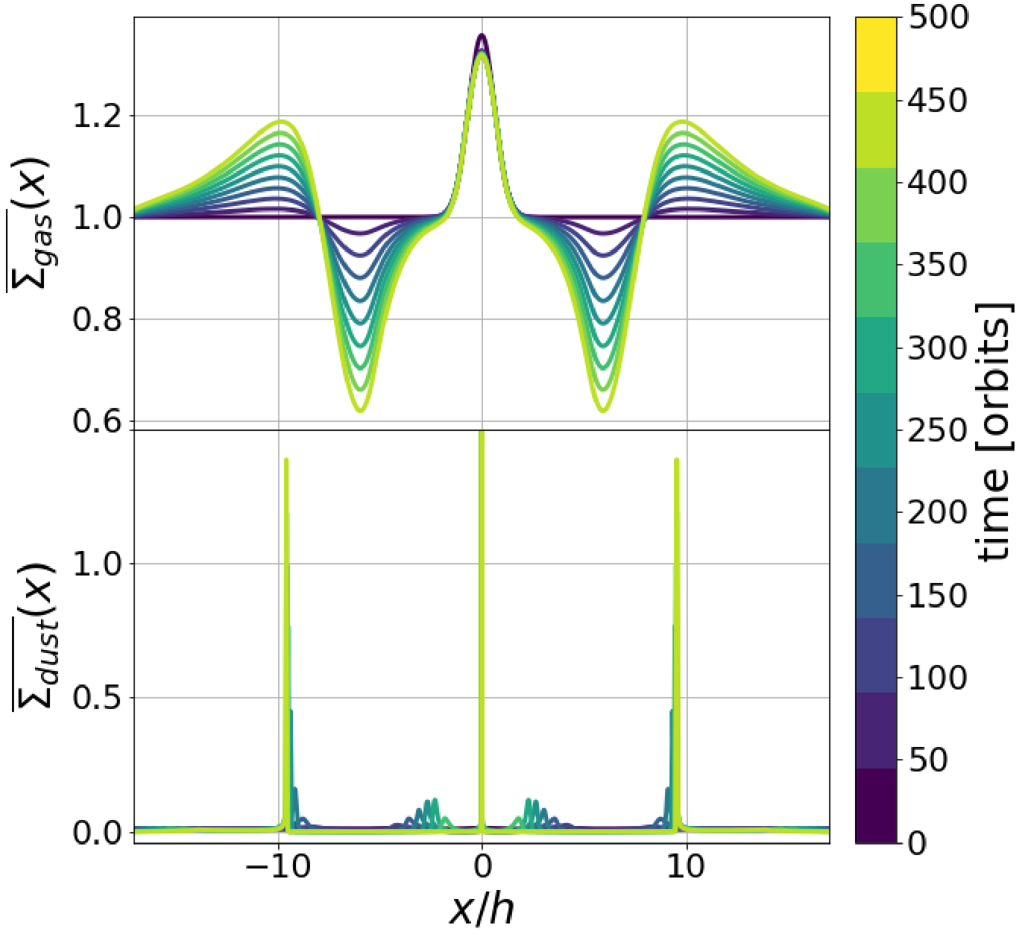

Figure 4.2: Radial density profiles of dust and gas at various time steps for model ‘A2’. The color bars indicate the corresponding time.

dust ring exhibits a slight outward migration as the simulation progresses, as depicted in Figure 5.3.

At t = 400 orbits, the gas gap is located at 5.9 h away from the vortex with a density contrast $\delta\Sigma_{\rm g}(x_{\rm gap})/\Sigma_{\rm g,0}(x_{\rm gap}) = 0.34$, illustrated in Figure 4.3. The location of the gas gap is defined as the local minimum of the gas surface density. On the edge of the gas gap, a pressure bump is formed. Due to the aerodynamic drag of gas, dust particles always drift in the direction of the pressure gradient. Therefore, the dust particles accumulate at the pressure bump located on the outer edge of the gas gap, resulting in a narrow dusty ring at $x_{\rm ring} = 9.5h$. Within this ring, there exists a significant density contrast, with $\delta\Sigma_{\rm d}(x_{\rm ring})/\Sigma_{\rm d,0}(x_{\rm ring}) = 118$, signifying that the density within the dusty ring is two orders of magnitude higher than the initial profile. The dust-to-gas ratio reaches unity inside the dust ring, $\delta\Sigma_{\rm d}(x_{\rm ring})/\Sigma_{\rm g}(x_{\rm ring}) \sim 1$. As dust diffusion is not accounted for in the simulation, the dust ring becomes increasingly narrow as the simulation progresses. However, the dust ring is spatially resolved through out the simulation.

Now that we have observed the formation of a gas gap and dusty ring in the simulation within hundreds of orbits. For an object orbiting a solar mass star at a distance of 100 AU, completing 400 orbits corresponds to approximately 0.4 Myr. The next step is to confirm that these substructures are indeed generated by the vortex.

4.2 Correlation between the location of shock wave and gas gap

The density waves induced by the vortex lead to the formation of gas gaps in the disk through shock dissipation. These shock waves disrupt the conservation of vortensity, manifesting as peaks in the radial profile of vortensity. Additionally, the shock waves transfer angular momentum to the local disk, resulting in a sharp decrease in the angular momentum flux carried by the waves. Thus, if the gap is indeed formed by the shock dissipation of vortex-induced density waves, its location should closely coincide with the peaks in vortensity and the cut-off in angular momentum flux.

Figure 4.4 displays the radial profiles of gas surface density, vortensity, and angular momentum flux carried by the density waves at 400 orbits. Vortensity is computed using Equation 3.16, while the angular momentum flux (AMF) is calculated using

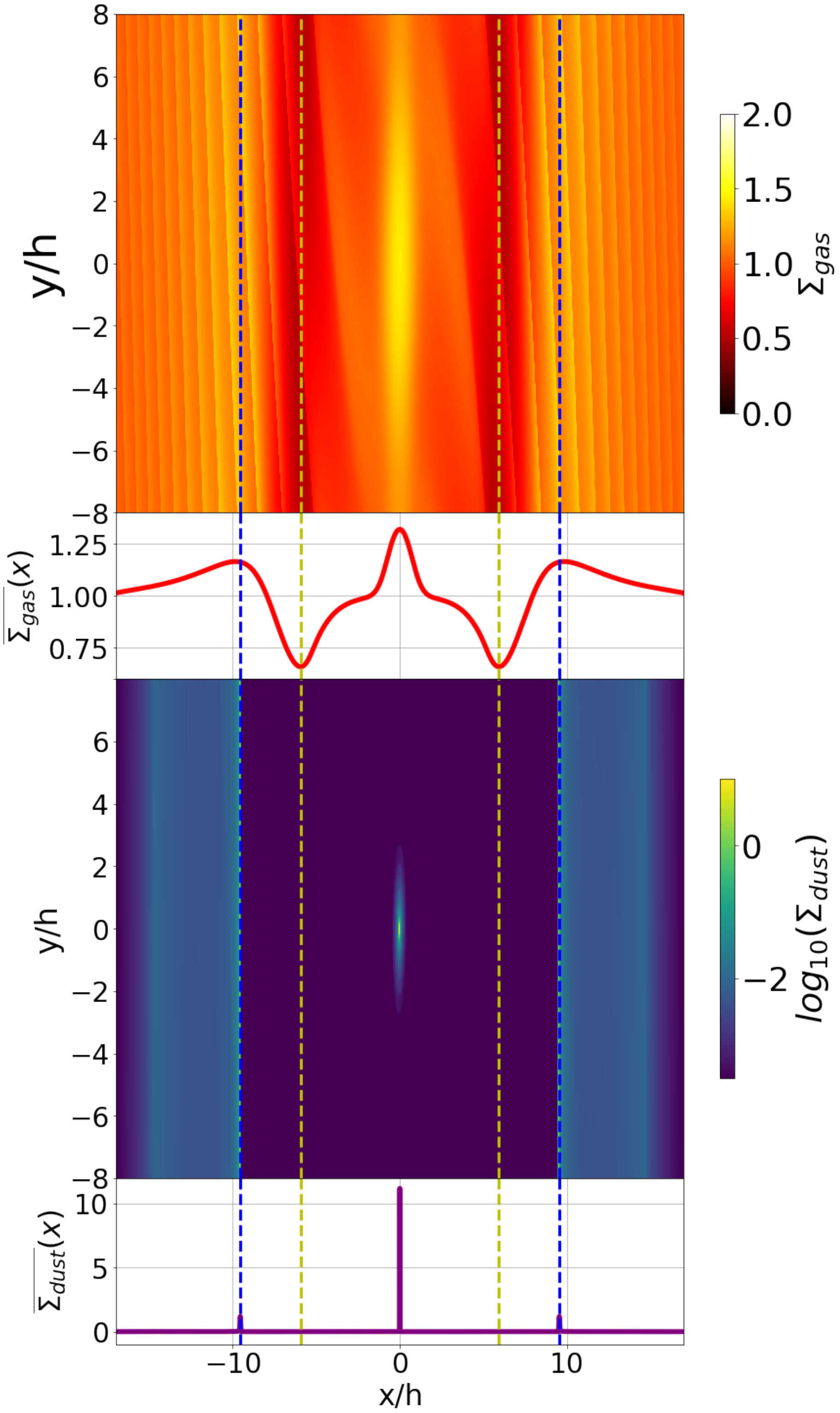

Figure 4.3: Surface density for gas (top) and dust (bottom) along with their radial profiles. The location of the dust ring is denoted by the blue dashed line, and the yellow dashed line indicates the location of the gas gap. The dusty ring forms at the pressure bump on the outer edge of the gas gap.

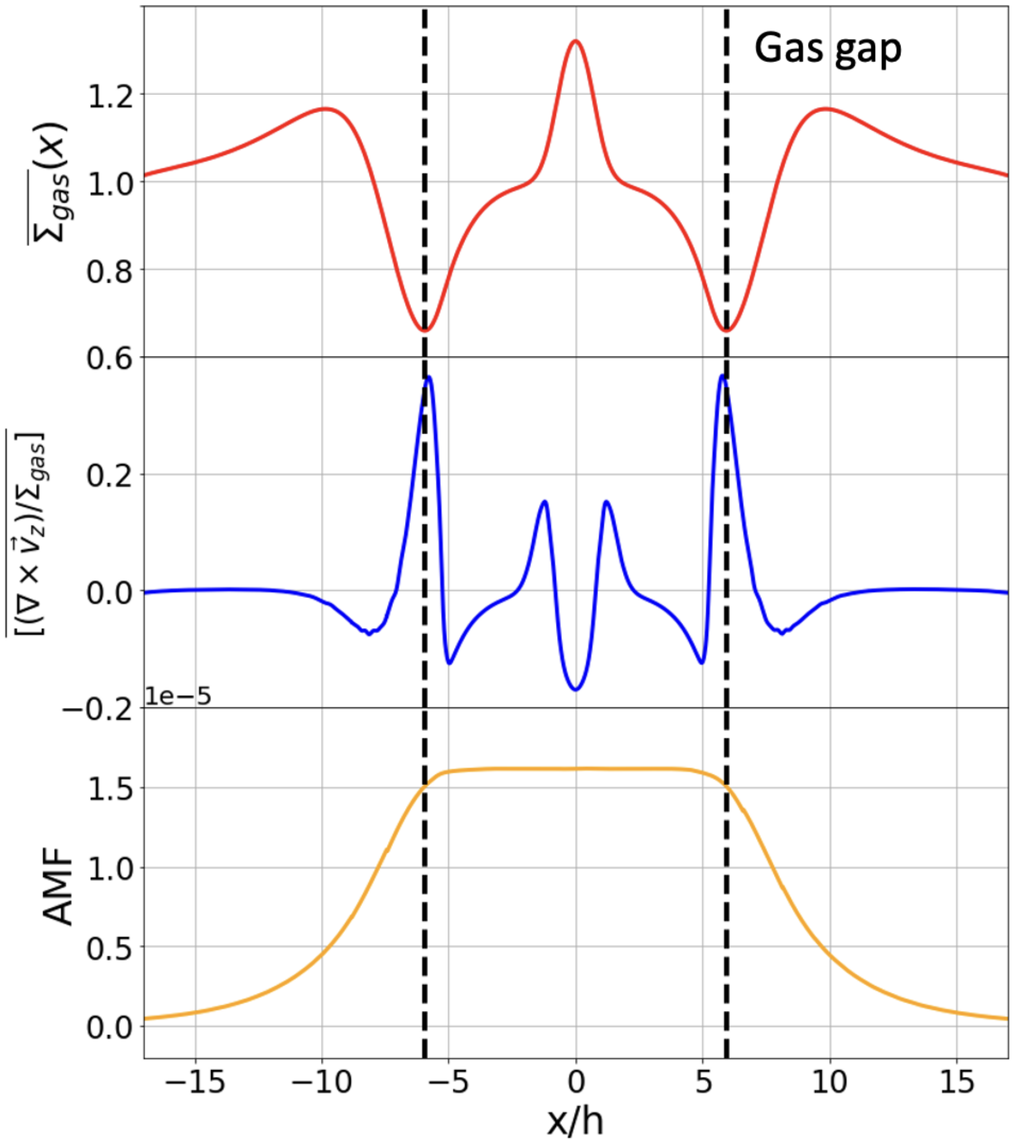

Figure 4.4: The radial profiles for the surface gas density (top), vortensity (middle), and angular momentum flux (bottom) for model 'A2' at $t = 400$ orbits. The black dashed line indicates the location of the gas gap, which is defined as the position of the local minimum of the surface gas density. Notably, the location of the gas gap aligns closely with both the peaks in vortensity and the cutoffs in angular momentum flux.

Equation 3.18. The location of the gas gap, denoted by the black dashed line, aligns with the peaks in vortensity and the cut-offs in the angular momentum flux, which are indicators of shock location for density waves. This consistency reveals that the gas gap is indeed formed by the shock dissipation of vortex-induced density waves. Consequently, we can conclude that such long-lived vortices can create rings and gaps within inviscid disks.

Chapter 5

Evaluation, Analysis and Comparisons

5.1 Vortex property

Previous studies indicate that the shape of the vortex significantly influences its strength. Circular vortices ($\chi \approx 1$) are stronger and generate density waves that carry more angular momentum flux [Paardekooper et al., 2010]. Consequently, circular vortices are more efficient in opening deeper gaps in the disk.

The growth rate of the RWI is inversely proportional to the aspect ratio of the vortex [Ono et al., 2018]. A steep density bump leads to a more unstable RWI [Ono et al., 2016], resulting in faster growth and the formation of more circular vortices. Therefore, different disk models, as listed in Table 3.1, will produce vortices with varying strengths.

In this section, we explore the relationship between the aspect ratio of the gaseous vortex and the properties of the induced substructures across various disk models.

5.1.1 Aspect ratio of the vortex

The semi-major $a_{\rm v}$ and semi-minor $b_{\rm v}$ axis of the gaseous vortex is calculated from the velocity profile of $\delta v_y(x, y_{\rm v})$ and $v_x(x_{\rm v}, y)$ of at the vortex center, as described in section 3.3.1.

Figure 5.1 plots the velocity profiles at the vortex center for the 'A2' disk model at at $t = \tau_{20}$, serving as an example. The semi-major axis for the gaseous vortex is $a_{\rm v} = 4.40h$, and the semi-minor axis is $b_{\rm v} = 0.95h$, resulting in an aspect ratio of the

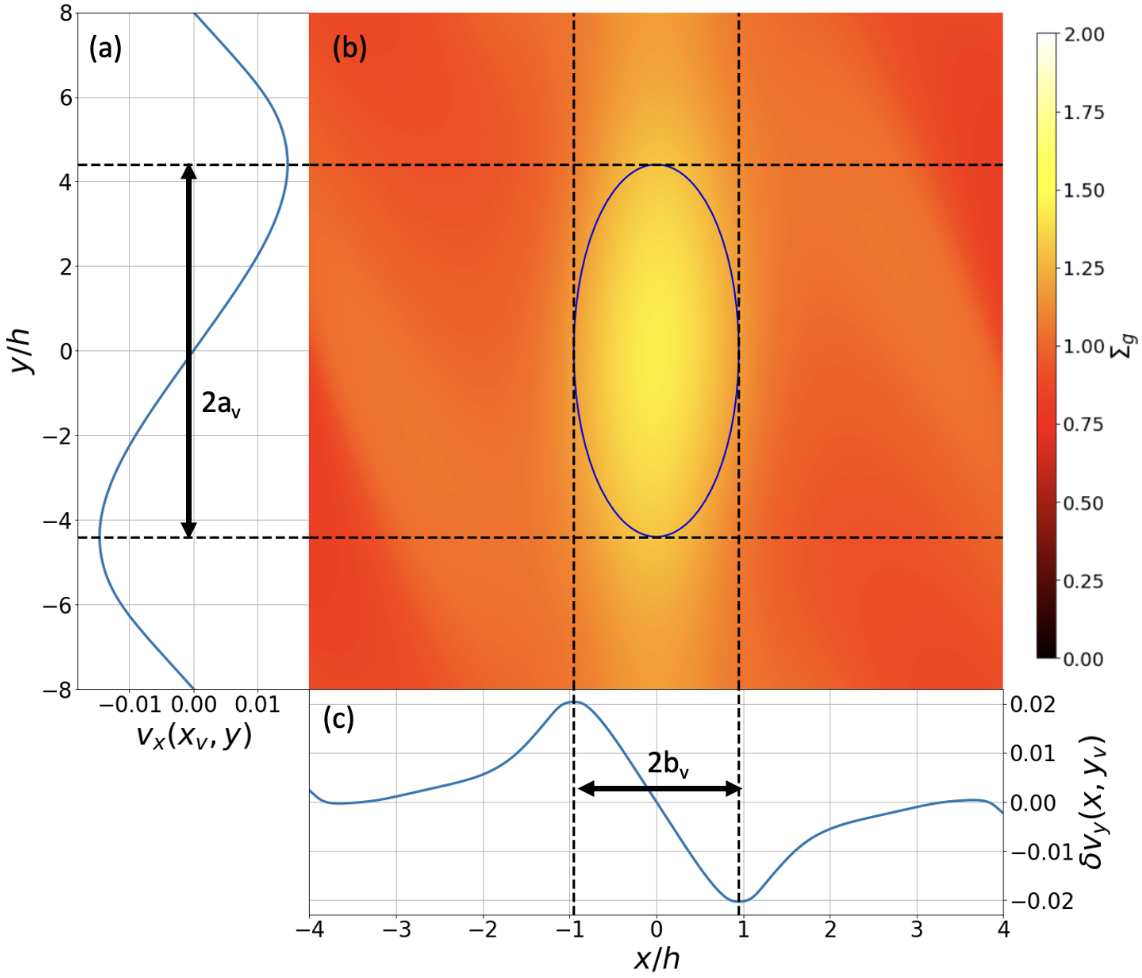

Figure 5.1: Radial velocity v_x along the y direction (a), surface gas density (b), and azimuthal velocity perturbation δv_y along the x direction (c) for the 'A2' disk model at $t = \tau_{20}$. Black dashed lines mark local extrema near the vortex. The distance between local maximum and minimum in v_x defines the major axis $2a_{\text{v}}$, while for δv_y it defines the minor axis $2b_{\text{v}}$. An ellipse, delineated by a_{v} and b_{v} from the velocity profile, represents the vortex shape in blue.

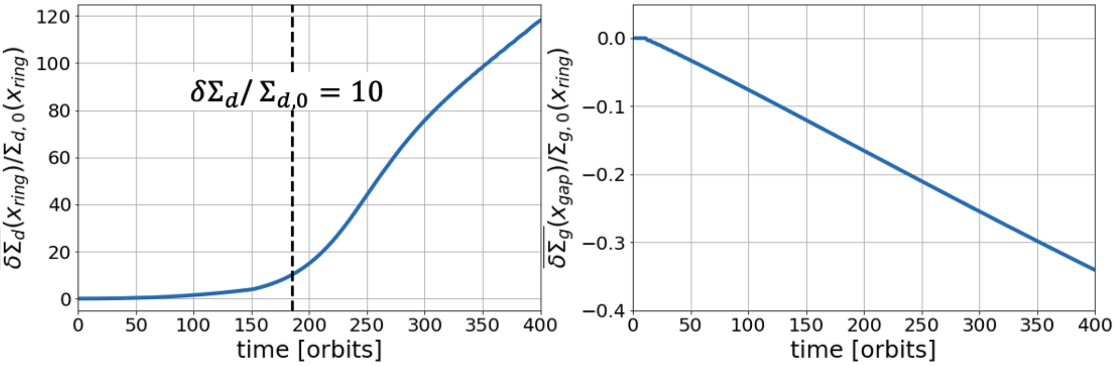

Figure 5.2: Evolution of dust density contrast at the dust ring (left) and gas density contrast at the gas gap (right). The black dashed line marks the point in time when the dust density at the ring becomes one order of magnitude higher than the initial background density.

vortex of $\chi = a_{\rm v}/b_{\rm v} = 4.63$.

5.1.2 Time evolution of vortex and substructure

The vortex typically reaches a quasi-stationary state after tens of orbits [Ono et al., 2018], remaining relatively stationary. While its radial size remains almost constant, its aspect ratio may vary over long timescales, spanning thousands of orbits [Ono et al., 2018]. However, for the duration of simulations in this work, which is less than 1000 orbits, roughly equivalent to one Myr for an object orbiting around a solar mass star at a distance of 100 AU, the aspect ratio of the vortex remains relatively constant.

Figure 5.2 illustrates the evolution of the density contrast at the dust ring and the gas gap. The depth of the gap increases almost linearly with respect to time. Dust accumulation at the ring accelerates as time progresses, and slightly slows down at later orbits when the dust grains within the disk are depleted .

We considered the dust ring to be fully formed once its density is one order of magnitude higher than the initial background density, shown as the black dash line in Figure 5.2. Once the ring is formed, its position is relatively stable which only slightly moves outwards by less than $1h$ as time progresses. The location of the gas gap is even more stable with respect to time, shown in Figure 5.3.

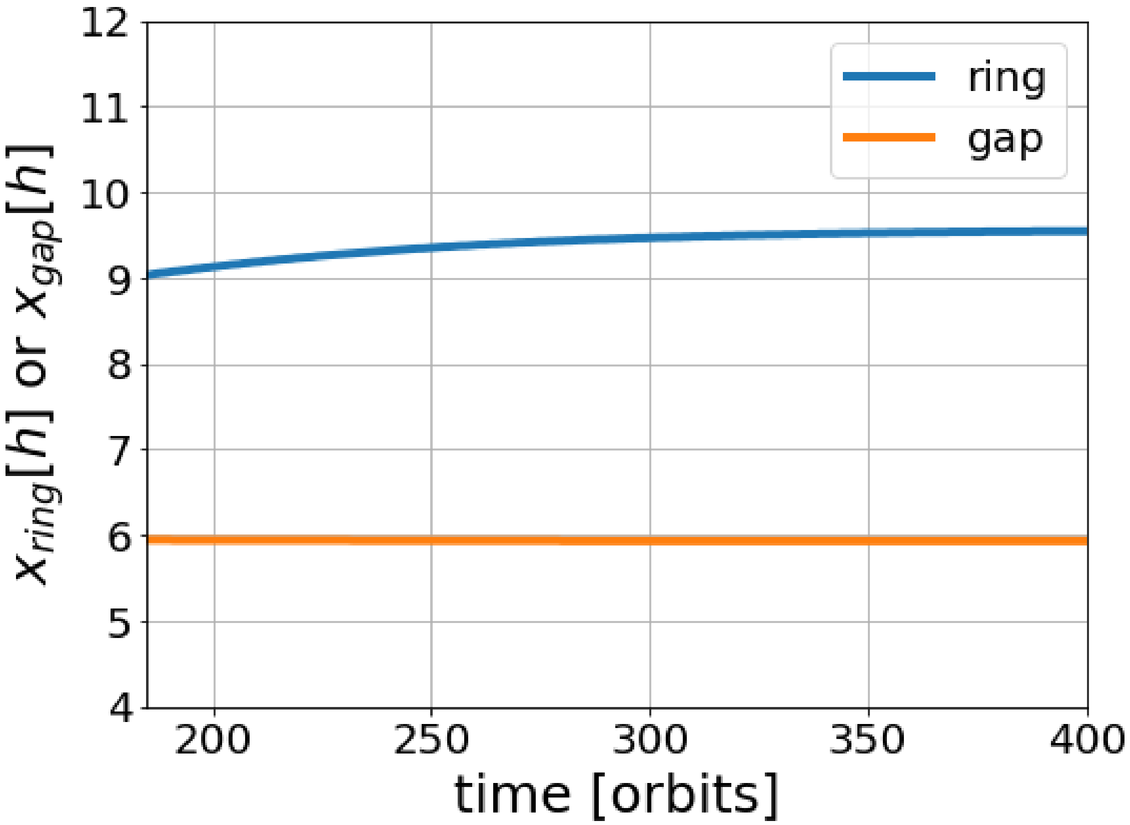

Figure 5.3: The evolution of the position of the dust ring and gas gap after the density at the dust ring reaches one order of magnitude higher than the background density. The blue line represents the evolution of the dust ring, while the orange line illustrates the evolution of the gas gap.

5.1.3 Comparison between different disk models

The ability of the vortex to generate rings and gaps relies heavily on its strength, which is influenced by the aspect ratio of the vortex. As a result, the timescale for ring formation varies significantly across different disk models.

Table 5.1 shows the time (τ_{10}) at which $\delta\Sigma_d/\Sigma_{d,0}$ reaches ∼10. As the amplitude of the initial density bump decreases, it leads to the formation of a weaker vortex, which requires a significantly longer time to form a dust ring. For disk model 'A2', it takes only 185 orbits to form a dust ring with a density contrast one order of magnitude higher than the background density, as indicated by the black dashed line in Figure 5.2. This time increases significantly to 730 orbits for a weaker disk model 'A4'. The dust ring reaches $\delta\Sigma_d/\Sigma_{d,0} \sim 20$ at 860 orbits, approaching the limit of the simulation duration.

Name	A_0	τ_{10} [orbits]	τ_{20} [orbits]	AMF (10^{-5})	χ	$x_{\rm ring}[h]$
A1	0.439	138	159	3.35	4.09	8.24
A2	0.358	185	212	1.57	4.63	9.20
A3	0.227	394	461	0.62	5.99	12.33
A4	0.205	730	860	0.17	8.28	16.88

Table 5.1: Characteristics of the disk models. We fix the width of the initial pressure bump and only vary its amplitude. This includes the timescales when $\delta\Sigma_d/\Sigma_{d,0}$ reaches ∼10 (τ_{10}) and ∼20 (τ_{20}), the angular momentum flux (AMF) at $t = \tau_{20}$, and the aspect ratio of the vortex (χ) at τ_{20}. $x_{\rm ring}$ denotes the position of the local maximum in the dust surface density at $t = \tau_{20}$.

The shape of the vortex also significantly influences its strength. For models with a stronger vortex, the aspect ratio of the vortex is smaller, as shown in the sixth column of Table 5.1, consistent with previous findings [Paardekooper et al., 2010]. Since the shape of the vortex remains relatively constant over hundreds of orbits, as discussed in section 5.1.2, we select the aspect ratio of the vortex at $t = \tau_{20}$, as it reflects the shape for the quasi-steady vortex throughout the simulation.

Previous work suggests that stronger vortices generate density waves that carry more angular momentum flux [Paardekooper et al., 2010], which is consistent with our simulation results. The fifth column of Table 5.1 presents the angular momentum flux carried by the wave before the shock, at $t = \tau_{20}$ for each model. The AMF is notably smaller for models with a lower-density bump and a weaker vortex.

Density waves that carry more angular momentum flux tend to have shorter shock

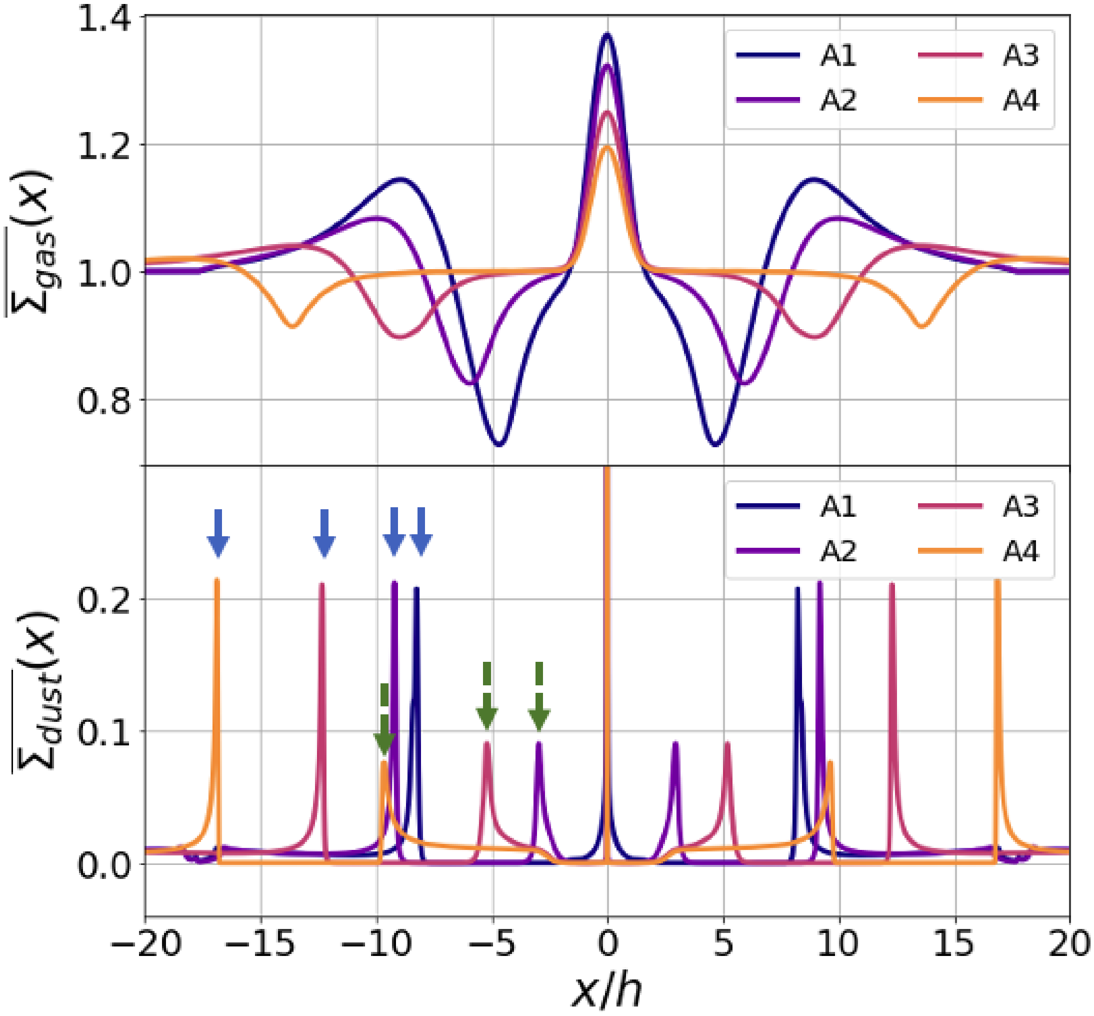

Figure 5.4: Radial density profiles for gas (top) and dust (bottom) of disk models at $t = \tau_{20}$. Weaker models show two distinct dust rings on each side of the vortex. Our focus is primarily on the outer rings (indicated by blue solid arrows), formed by dust accumulation at the pressure bump along the outer edge of the gas gap. Inner rings (marked by green dashed arrows) arise from dust gathering at a shallower pressure bump along the inner edge of the gas gap. Over time, the inner dust ring gradually fades as dust particles migrate inward into the vortex, as illustrated in Figure 4.2.

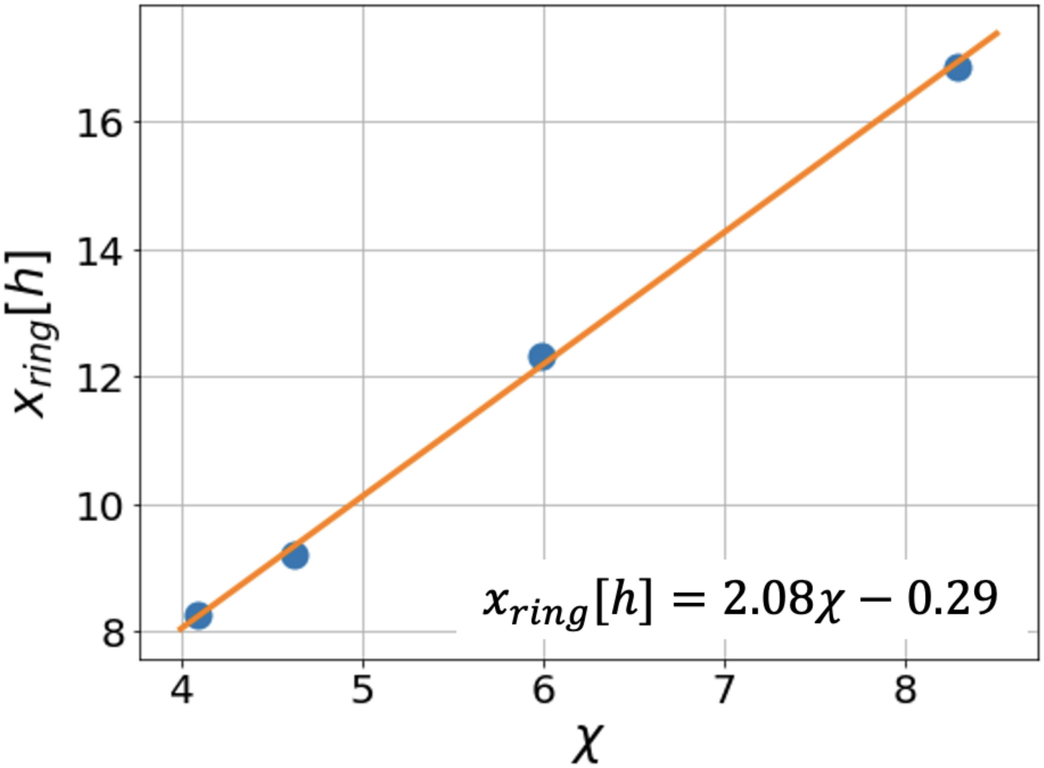

Figure 5.5: Empirical relation between the aspect ratio of the gaseous vortex and the location of the dust ring. The blue dots represent the dust ring positions listed in Table 5.1, and the orange line represents the linear empirical relation derived from curve-fitting.

distances. Therefore, a strong vortex that generates density waves carrying more angular momentum flux experience a shorter shock distance. Since the position of the gas gap closely aligns with the shock location, a stronger vortex will produce a gas gap that is closer to itself, and consequently, a closer dust ring. We have observed such trend in our simulations. Figure 5.4 displays the radial density profiles for dust and gas at $t = \tau_{20}$ for each model, indicating that the outer dust ring is further away from the vortex for models with weaker vortex.

Given that the strength of the vortex is directly related to the aspect ratio of the gaseous vortex, there exists a correlation between the aspect ratio of the gaseous vortex and the position of the dust ring. Theoretically, a circular vortex will produce a dust ring that is closer to itself.

To empirically establish the relationship between the aspect ratio of the gaseous vortex and the position of the dust ring, we conduct a curve-fit analysis using these parameters. Specifically, we focus on the dust ring position at $t = \tau_{20}$, as listed in Table 5.1. Even though the dust ring does not reach full stability at $t = \tau_{20}$, as depicted in Figure 5.3, where it continues to shift outward post τ_{20}, the vortex's displacement is minimal, changing by merely $\sim 0.3h$ over 200 orbits.

Figure 5.5 shows the linear empirical relationship we found by curve-fit, defined as below:

$$x_{\rm ring}/h = 2.08\chi - 0.29 \tag{5.1}$$

where $x_{\rm ring}$ is the location of the dust ring in the unit of disk scale height h and χ is the aspect ratio of the gas vortex. Using Equation 5.1, we can estimate the dust ring location based on the shape of the gaseous vortex. Future observations that incorporate both dust and gas emissions of the vortex can help validate this empirical relation. Such validation may have the potential to provide insights into whether the observed substructures are primarily generated by the vortex or other mechanisms, such as embedded planets.

Given the similarity between the density wave induced by a planet and the vortex, there exists an analogy between the strength of the vortex (expressed as its aspect ratio) and the mass of the planet. Utilizing the solution for inviscid Burger's equation under weak nonlinearity assumptions, we calculate the mass of planets that generate density waves shocked at the same distance as the vortices, employing Equation 8 in [Dong et al., 2011a], with $\gamma = 1.4$. Figure 5.6 illustrates the relationship between the aspect ratio of the vortex and its shock location, alongside the correlation between the aspect ratio and the mass of planets with the same shock distance. The planet mass is in the unit of thermal mass $M_{th} = c_s^3/G\Omega_P$, where the planet's Hill radius equals the scale height of the gas disk [Rafikov, 2006]. As expected, stronger and more circular vortices correspond to more massive planets. Generally, the vortices considered in this study correspond to lower mass planets with $M_p \ll M_{th}$.

5.1.4 Limitation of the empirical relation

As dust diffusion is not accounted for in the shearing box simulation, the dust particles become highly concentrated at the vortex center. The shape of the dust vortex never reaches a steady state; instead, it continuously shrinks. We are only able to determine the aspect ratio of the vortex in the gas component. Consequently, observations that capture both gas and dust emissions of the vortex are necessary to apply

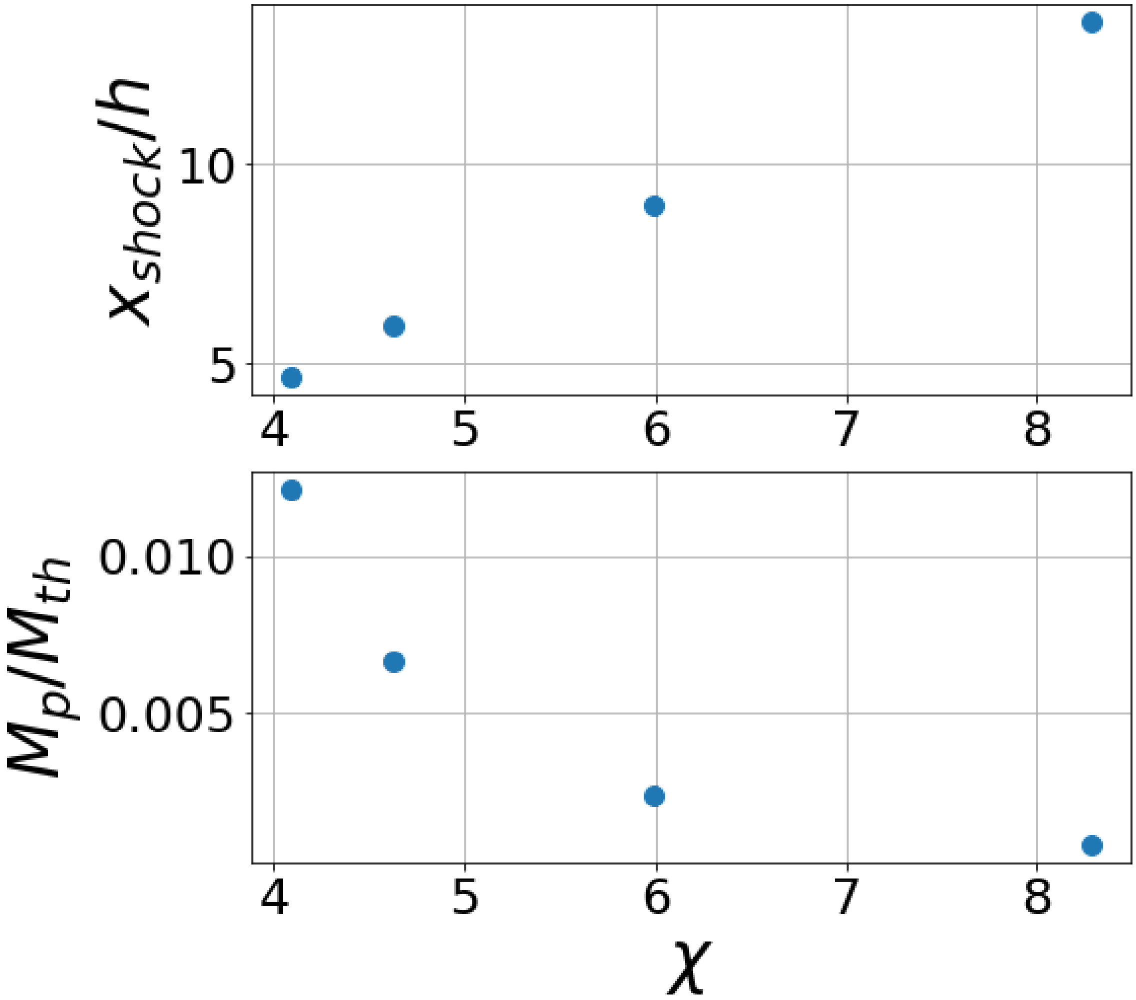

Figure 5.6: Relationship between the aspect ratio of the vortex and its shock location, estimated by the gas gap location (top), and the correlation between the aspect ratio and the mass of a planet with the same shock distance (bottom).

the empirical relation provided by Equation 5.1. Although recent observations have revealed azimuthal asymmetries in the dust continuum emission, no observations have yet shown the presence of crescents in gas emission. The signature of the vortex tends to be weak in gas emission with sufficient low local surface density compared to dust, making it easily overlooked [Huang et al., 2018, van der Marel et al., 2020]. However, the anticyclonic feature of the vortex can be detected with careful consideration of the source and observation setup [Huang et al., 2018] . Therefore, there is a possibility that this empirical relation could be applied to future observations.

This empirical relation is derived within a shearing box framework, neglecting the influence of vortex migration, curvature of the disk and viscosity. In a more realistic global disk, vortices will migrate inward, and the migration rate also relates to the aspect ratio of the vortex. Stronger, circular vortices tend to migrate faster than weaker ones [Paardekooper et al., 2010, Ono et al., 2018]. Consequently, both the shock location and the position of the dust ring may shift due to vortex migration. Additionally, the viscosity causes the dissipation of angular momentum to happen earlier and smooth out the vortensity peak [Dong et al., 2011a]. Therefore, it is possible that the empirical relation may not hold in a global disk setting with viscocity. Future work is necessary to further constrain the relationship in a more realistic global disk model and compare it with real observations.

5.2 Synthetic image and observations

To ascertain the detectability of the dust ring produced by the vortex in real observations, we generate an ALMA synthetic image from the dust surface density obtained from the global simulation of the 'A2' disk model, using the stellar parameters of the disk HD 135344B [Cazzoletti et al., 2018]. This process is detailed in Section 3.4. The resulting simulated dust surface density and the corresponding synthetic image are presented in Figure 5.7, showcasing the presence of an inner ring and a brighter outer crescent.

While recent observations have revealed that several disks exhibit large cavities and azimuthal asymmetries [van der Marel et al., 2020], only a few disks display both asymmetries and dust rings, such as HD 135344B, also known as SAO 206462 [van der Marel et al., 2016] and HD 143006 [Pérez et al., 2018, Andrews et al., 2018].

HD 135344B features an inner dust cavity with smaller ^{13}CO and C^{18}O gas cavity [van der Marel et al., 2015]. It also exhibits an inner ring and outer azimuthal

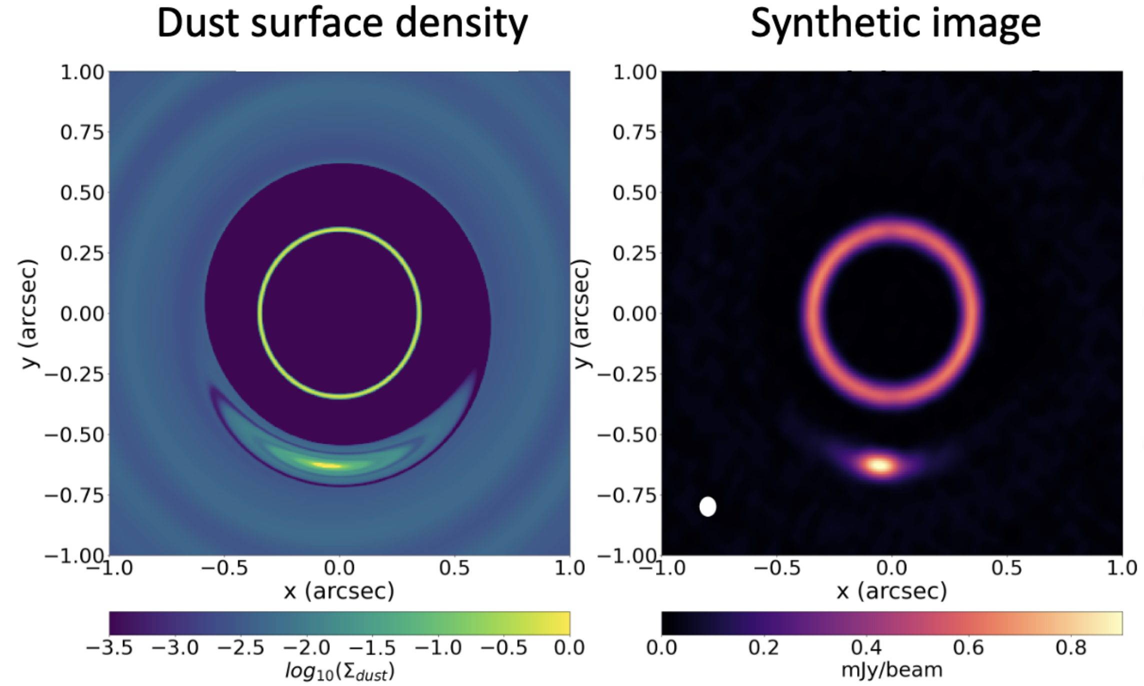

Figure 5.7: *left*: Dust surface density from the global simulation for the disk model 'A2' at $t = 417$ orbits. *right*: Synthetic images at 1.9 mm are shown corresponding to the simulation. The white ellipse in the bottom left corner of the synthetic image represents the beam size of 0.079" × 0.070".

asymmetry in dust continuum observations [van der Marel et al., 2016], along with two spiral arms in scattering light [Muto et al., 2012]. Multi-wavelength observations have detected the presence of larger dust grains at the center of the vortex, the azimuthal shift of the vortex peak with wavelength, and the greater azimuthal concentration of the asymmetry at longer wavelengths [Cazzoletti et al., 2018], which aligns with the theoretical predictions for vortex nature of the asymmetric structure. Therefore, this disk presents strong evidences that the azimuthal asymmetry is caused by a vortex. Although the ring is closer to the vortex and the azimuthal asymmetry more extended in dust continuum emission for HD 135344B, the ALMA observation at Band 4 exhibits similar features to our synthetic image: an inner ring and a brighter crescent in the outer disk. Hence, there exists a possibility that the inner dust ring in the disk is generated by the vortex mechanism studied in this work, provided that it might be feasible for the vortex to produce observable rings and gaps in real discs.

However, the morphology of HD 143006 is more complex. The disk consists of three inner rings, a bright asymmetry in the outer disk, and there is a misalignment between the inner and outer disk in the dust continuum [Pérez et al., 2018, Andrews et al., 2018]. The asymmetry and misalignment are also observed in scattering light observations [Benisty et al., 2018]. The substructures observed in HD 143006 are likely produced by a combination of factors, including a misaligned central binary and an embedded planet aligned with the outer disk [Ballabio et al., 2021]. It is unlikely that such complex substructures are solely produced by a vortex, but there is a possibility that vortex-induced density waves also contribute to the formation of the rings.

5.3 Feasibility for vortex-disk interaction

In this work, we examine the simplest disk setup to assess the capability of a long-lived vortex in generating observable rings and gaps within an inviscid disk. This serves as the first step towards investigating vortex-disk interactions. Notably, several critical physical effects such as viscosity, self-gravity, 3D dynamics, and dust feedback have not been included in our simulations. In this section, we address the feasibility of vortex-disk interactions to produce observable rings and gaps in a more realistic disk environment, accounting for multiple physical effects. Specifically, we discuss how these effects may influence vortex longevity and the lifetime of induced structures.

5.3.1 Viscosity

In general, viscosity acts diffusively to smooth out sharp radial gradients in the disk surface density, counteracting the tendency of angular momentum transport in the gap-opening process [Armitage, 2020, Dong et al., 2011a]. Therefore, in disks with high viscosity, it becomes more challenging for the vortex to open up a gas gap and produce dust rings. Moreover, viscosity also significantly affects the RWI. A viscosity parameter of $\alpha \lesssim 10^{-4}$ is required to sustain a long-lived vortex [Godon and Livio, 1999, Fu et al., 2014a]. We expect such a scenario of low viscosity can be achieved within the MRI dead zones, where the disk is poorly ionized and the MRI is inactive [Gammie, 1996].

However, for RWI triggered at the edges of dead zones, the vortex can persist with higher viscosity, the extent of which depends on the width of the dead zone [Regály et al., 2011, Li and Li, 2015]. Notably, once RWI is triggered, the dead zone does not decay, allowing the vortex to periodically reform in low-viscosity disks [Tarczay-Nehéz et al., 2021, Li and Li, 2015].

Overall, it is more challenging for the vortex to survive and induce substructure in the disk with high viscosity.

5.3.2 Vortex Longevity

In the global disk, vortices induce density waves with an imbalance torque on each side due to geometric effects, leading to radial migration inward, similar to Type I migration for planets [Paardekooper et al., 2010]. The migration timescale strongly depends on the aspect ratio of the vortex. Circular vortices migrate much faster than elongated ones. Typically, the vortex migration timescale is around 1-10 Myr, unless the aspect ratio is smaller than 4 or the vortex has a radial size larger than $2h$ [Ono et al., 2018]. Even with this migration, vortices can persist within the disk for a significant duration. Consequently, migration is not expected to significantly affect their ability to produce rings and gaps. However, it can alter the shock location, potentially resulting in shallower gaps and giving rise to multi-ring and gap features.

RWI is inherently a 2D instability. Linear analysis of RWI in 3D disks indicates that the mode growth rate in 3D is similar to that in 2D [Meheut et al., 2012]. The formation of a vortex exhibits similarities in both 3D and 2D scenarios. Nonetheless, in 3D, the emergence of elliptical instability can lead to the destruction of vortices with small aspect ratios ($\chi \leq 4$) [Lesur and Papaloizou, 2009, Richard et al., 2013]. Consequently, it may be more challenging for vortices to persist in 3D scenarios.

For the disk with self-gravity, the excited density waves carry larger angular momentum flux resulting in deeper gaps in more massive discs [Zhang and Zhu, 2020]. However, self-gravity hinders the initiation of RWI with low azimuthal modes according to linear theory [Lovelace and Hohlfeld, 2012]. Simulations also reveal that RWI vortices are weakened by self-gravity, which takes longer to form a fully developed vortex [Baruteau and Zhu, 2016]. Furthermore, self-gravity significantly influences vortex evolution within the disk. In low-mass disks with self-gravity, vortices decay due to self-gravitational torques [Pierens and Lin, 2018]. Conversely, in more massive disks, vortices develop gravitational instabilities within their cores, allowing 3D vortices to survive against the elliptic instabilities for a longer lifetime [Lin and Pierens, 2018].

The impact of dust feedback is negligible when the dust-to-gas ratio is relatively low (on the order of 10^{-2}). Therefore, we can safely disregard dust feedback in most parts of the simulation domain, except in regions of high dust concentration such as the vortex center and the dust ring. Vortices can effectively trap dust particles, leading to a sufficiently high dust-to-gas ratio at the vortex center. As the density of dust particles approaches gas density within the vortex, the effects of dust drag on gas motion become significant. At this point, a dynamical instability can be triggered, leading to the destruction of the vortex [Fu et al., 2014b].

5.3.3 Dust ring lifetime

For a low-viscosity disk with $\alpha \lesssim 10^{-4}$, the local viscous timescale as h^2/ν might be longer than the lifetime of the vortex. When the vortex dissipates or migrates away, the gas gap and dust ring may persist for some time before the pressure bump at the gap's edge is smoothed out by turbulence and viscosity. Viscous diffusion gradually releases dust grains trapped in the pressure bump, leading to radial drift until the dust ring eventually dissipates. Higher viscosity in the disk accelerates the vanishing of the dust ring [Kanagawa et al., 2021].

Additionally, the dust-to-gas ratio within the dust ring can be sufficiently high, triggering significant dust feedback effects. This feedback can induce mesoscale instabilities, resulting in clumpy rings with compact regions of higher density [Huang et al., 2020]. Pebble-sized particles within clumpy rings experience minimal radial drift due to dust-to-gas feedback. These clumpy dust rings may persist without the pressure bump as long as there is a high external mass flux feeding into the ring to support planetesimal formation [Jiang and Ormel, 2021].

Therefore, even in disks where a crescent is not observed in the dust continuum, it remains possible that the rings were initially generated by the vortex but dissipated due to migration or other factors mentioned in the previous Section 5.3.2.

Chapter 6

Conclusions

In this work, we explore a novel mechanism for the generation of rings and gaps through the influence of vortex-induced density waves within protoplanetary disks. Through hydrodynamic simulations, vortex property analysis, and radiative transfer modeling, we investigate the interactions between long-lived vortices and the disk, enhancing our understanding of structure formation.

The key findings of our study are outlined below:

- Hydrodynamic simulations conducted in a shearing box, along with analysis of density waves induced by long-lived RWI vortices, have confirmed the capacity of these waves to transport angular momentum through shock dissipation, and form gas gaps and dust rings within the inviscid disk.
- We have established an empirical relationship between the aspect ratio of the gaseous vortex and the location of the dust ring, derived from simulations across different disk models. Despite some limitations, this relationship serves as a foundation for future observational studies to verify whether these structures are indeed generated by vortices.
- Utilizing radiative transfer, we have generated a synthetic image of global simulations that closely resemble real observations, thus verifying the detectability of vortex-induced rings in ALMA observations.

While our study confirms the capability of long-lived vortices to generate rings and gaps within the inviscid disk, it represents just the first step in understanding the mechanism behind vortex-induced structures within the disk. It is essential to recognize the inherent limitations of our simulation approach, which primarily revolves around simplified disk conditions. Future research should delve into the vortex-disk interaction across a more intricate parameter space to mitigate these limitations.

By uncovering the influence of vortex-induced density waves on the formation of rings and gaps, we have offered a new mechanism for the origin of these substructures, highlighting mechanisms independent of planetary presence. Our findings deliver an essential message: when encountering ring structures in observations, it is possible that these features might not be attributable to planet-disk interaction but rather vortex-disk interaction. Our work provides insights into the evolution of protoplanetary disks and the underlying processes of planet formation.

Bibliography

[Andrews, 2020] Andrews, S. M. (2020). Observations of protoplanetary disk structures. *Annual Review of Astronomy and Astrophysics*, 58(1):483–528.

[Andrews et al., 2018] Andrews, S. M., Huang, J., Pérez, L. M., Isella, A., Dullemond, C. P., Kurtovic, N. T., Guzmán, V. V., Carpenter, J. M., Wilner, D. J., Zhang, S., Zhu, Z., Birnstiel, T., Bai, X.-N., Benisty, M., Hughes, A. M., Öberg, K. I., and Ricci, L. (2018). The Disk Substructures at High Angular Resolution Project (DSHARP). I. Motivation, Sample, Calibration, and Overview. , 869(2):L41.

[Armitage, 2017] Armitage, P. J. (2017). Physical processes in protoplanetary disks.

[Armitage, 2020] Armitage, P. J. (2020). *Astrophysics of Planet Formation*. Cambridge University Press, 2 edition.

[Bai and Stone, 2014] Bai, X.-N. and Stone, J. M. (2014). Magnetic flux concentration and zonal flows in magnetorotational instability turbulence. *The Astrophysical Journal*, 796(1):31.

[Ballabio et al., 2021] Ballabio, G., Nealon, R., Alexander, R. D., Cuello, N., Pinte, C., and Price, D. J. (2021). Hd 143006: circumbinary planet or misaligned disc? *Monthly Notices of the Royal Astronomical Society*, 504(1):888–897.

[Baruteau and Zhu, 2016] Baruteau, C. and Zhu, Z. (2016). Gas and dust hydrodynamical simulations of massive lopsided transition discs – ii. dust concentration. *Monthly Notices of the Royal Astronomical Society*, 458(4):3927–3941.

[Benisty et al., 2018] Benisty, M., Juhász, A., Facchini, S., Pinilla, P., de Boer, J., Pérez, L. M., Keppler, M., Muro-Arena, G., Villenave, M., Andrews, S., Dominik, C., Dullemond, C. P., Gallenne, A., Garufi, A., Ginski, C., and Isella, A. (2018).

Shadows and asymmetries in the t tauri disk hd 143006: evidence for a misaligned inner disk. *Astronomy amp; Astrophysics*, 619:A171.

[Birnstiel et al., 2010] Birnstiel, T., Dullemond, C. P., and Brauer, F. (2010). Gas- and dust evolution in protoplanetary disks. *Astronomy and Astrophysics*, 513:A79.

[Birnstiel et al., 2018] Birnstiel, T., Dullemond, C. P., Zhu, Z., Andrews, S. M., Bai, X.-N., Wilner, D. J., Carpenter, J. M., Huang, J., Isella, A., Benisty, M., Pérez, L. M., and Zhang, S. (2018). The disk substructures at high angular resolution project (dsharp). v. interpreting alma maps of protoplanetary disks in terms of a dust model. *The Astrophysical Journal Letters*, 869(2):L45.

[Cazzoletti et al., 2018] Cazzoletti, P., van Dishoeck, E. F., Pinilla, P., Tazzari, M., Facchini, S., van der Marel, N., Benisty, M., Garufi, A., and Pérez, L. M. (2018). Evidence for a massive dust-trapping vortex connected to spirals: Multi-wavelength analysis of the hd 135344b protoplanetary disk. *Astronomy amp; Astrophysics*, 619:A161.

[Cimerman and Rafikov, 2021] Cimerman, N. P. and Rafikov, R. R. (2021). Planet-driven density waves in protoplanetary discs: Numerical verification of non-linear evolution theory. *Monthly Notices of the Royal Astronomical Society*, 508(2):2329–2349.

[Currie et al., 2022] Currie, T., Lawson, K., Schneider, G., Lyra, W., Wisniewski, J., Grady, C., Guyon, O., Tamura, M., Kotani, T., Kawahara, H., Brandt, T., Uyama, T., Muto, T., Dong, R., Kudo, T., Hashimoto, J., Fukagawa, M., Wagner, K., Lozi, J., Chilcote, J., Tobin, T., Groff, T., Ward-Duong, K., Januszewski, W., Norris, B., Tuthill, P., van der Marel, N., Sitko, M., Deo, V., Vievard, S., Jovanovic, N., Martinache, F., and Skaf, N. (2022). Images of embedded jovian planet formation at a wide separation around ab aurigae. *Nature Astronomy*, 6(6):751–759.

[Dominik et al., 2021] Dominik, C., Min, M., and Tazaki, R. (2021). OpTool: Command-line driven tool for creating complex dust opacities. Astrophysics Source Code Library, record ascl:2104.010.

[Dong et al., 2011a] Dong, R., Rafikov, R. R., and Stone, J. M. (2011a). Density Waves Excited by Low-mass Planets in Protoplanetary Disks. II. High-resolution Simulations of the Nonlinear Regime. , 741(1):57.

[Dong et al., 2011b] Dong, R., Rafikov, R. R., Stone, J. M., and Petrovich, C. (2011b). Density Waves Excited by Low-mass Planets in Protoplanetary Disks. I. Linear Regime. , 741(1):56.

[Drażkowska and Alibert, 2017] Drażkowska, J. and Alibert, Y. (2017). Planetesimal formation starts at the snow line. *Astronomy amp; Astrophysics*, 608:A92.

[Dullemond et al., 2012] Dullemond, C. P., Juhasz, A., Pohl, A., Sereshti, F., Shetty, R., Peters, T., Commercon, B., and Flock, M. (2012). RADMC-3D: A multi-purpose radiative transfer tool. Astrophysics Source Code Library, record ascl:1202.015.

[Fu et al., 2014a] Fu, W., Li, H., Lubow, S., and Li, S. (2014a). Long-term Evolution of Planet-induced Vortices in Protoplanetary Disks. , 788(2):L41.

[Fu et al., 2014b] Fu, W., Li, H., Lubow, S., Li, S., and Liang, E. (2014b). Effects of Dust Feedback on Vortices in Protoplanetary Disks. , 795(2):L39.

[Fung and Ono, 2021] Fung, J. and Ono, T. (2021). Cooling-induced vortex decay in keplerian disks. *The Astrophysical Journal*, 922(1):13.

[Gammie, 1996] Gammie, C. F. (1996). Layered Accretion in T Tauri Disks. , 457:355.

[Godon and Livio, 1999] Godon, P. and Livio, M. (1999). Vortices in Protoplanetary Disks. , 523(1):350–356.

[Goodman and Rafikov, 2001] Goodman, J. and Rafikov, R. R. (2001). Planetary Torques as the Viscosity of Protoplanetary Disks. , 552(2):793–802.

[Haffert et al., 2019] Haffert, S. Y., Bohn, A. J., de Boer, J., Snellen, I. A. G., Brinchmann, J., Girard, J. H., Keller, C. U., and Bacon, R. (2019). Two accreting protoplanets around the young star pds 70. *Nature Astronomy*, 3(8):749–754.

[Hammond et al., 2023] Hammond, I., Christiaens, V., Price, D. J., Toci, C., Pinte, C., Juillard, S., and Garg, H. (2023). Confirmation and keplerian motion of the gap-carving protoplanet hd 169142 b. *Monthly Notices of the Royal Astronomical Society: Letters*, 522(1):L51–L55.

[Huang and Bai, 2022] Huang, P. and Bai, X.-N. (2022). A multifluid dust module in athena++: Algorithms and numerical tests. *The Astrophysical Journal Supplement Series*, 262(1):11.

[Huang et al., 2018] Huang, P., Isella, A., Li, H., Li, S., and Ji, J. (2018). Identifying anticyclonic vortex features produced by the rossby wave instability in protoplanetary disks. *The Astrophysical Journal*, 867(1):3.

[Huang et al., 2020] Huang, P., Li, H., Isella, A., Miranda, R., Li, S., and Ji, J. (2020). Meso-scale instability triggered by dust feedback in dusty rings: Origin and observational implications. *The Astrophysical Journal*, 893(2):89.

[Jiang and Ormel, 2021] Jiang, H. and Ormel, C. W. (2021). Survival of alma rings in the absence of pressure maxima. *Monthly Notices of the Royal Astronomical Society*, 505(1):1162–1179.

[Johansen et al., 2009] Johansen, A., Youdin, A., and Klahr, H. (2009). Zonal flows and long-lived axisymmetric pressure bumps in magnetorotational turbulence. *The Astrophysical Journal*, 697(2):1269–1289.

[Kanagawa et al., 2021] Kanagawa, K. D., Muto, T., and Tanaka, H. (2021). Dust Rings as a Footprint of Planet Formation in a Protoplanetary Disk. , 921(2):169.

[Keppler et al., 2018] Keppler, M., Benisty, M., Müller, A., Henning, T., van Boekel, R., Cantalloube, F., Ginski, C., van Holstein, R. G., Maire, A.-L., Pohl, A., Samland, M., Avenhaus, H., Baudino, J.-L., Boccaletti, A., de Boer, J., Bonnefoy, M., Chauvin, G., Desidera, S., Langlois, M., Lazzoni, C., Marleau, G.-D., Mordasini, C., Pawellek, N., Stolker, T., Vigan, A., Zurlo, A., Birnstiel, T., Brandner, W., Feldt, M., Flock, M., Girard, J., Gratton, R., Hagelberg, J., Isella, A., Janson, M., Juhasz, A., Kemmer, J., Kral, Q., Lagrange, A.-M., Launhardt, R., Matter, A., Ménard, F., Milli, J., Mollière, P., Olofsson, J., Pérez, L., Pinilla, P., Pinte, C., Quanz, S. P., Schmidt, T., Udry, S., Wahhaj, Z., Williams, J. P., Buenzli, E., Cudel, M., Dominik, C., Galicher, R., Kasper, M., Lannier, J., Mesa, D., Mouillet, D., Peretti, S., Perrot, C., Salter, G., Sissa, E., Wildi, F., Abe, L., Antichi, J., Augereau, J.-C., Baruffolo, A., Baudoz, P., Bazzon, A., Beuzit, J.-L., Blanchard, P., Brems, S. S., Buey, T., De Caprio, V., Carbillet, M., Carle, M., Cascone, E., Cheetham, A., Claudi, R., Costille, A., Delboulbé, A., Dohlen, K., Fantinel, D., Feautrier, P., Fusco, T., Giro, E., Gluck, L., Gry, C., Hubin, N., Hugot, E., Jaquet, M., Le Mignant, D., Llored, M., Madec, F., Magnard, Y., Martinez, P., Maurel, D., Meyer, M., Möller-Nilsson, O., Moulin, T., Mugnier, L., Origné, A., Pavlov, A., Perret, D., Petit, C., Pragt, J., Puget, P., Rabou, P., Ramos, J., Rigal, F., Rochat, S., Roelfsema, R., Rousset, G., Roux, A., Salasnich, B., Sauvage, J.-F., Sevin, A., Soenke, C., Stadler, E., Suarez, M., Turatto, M., and Weber, L. (2018). Discovery of a planetary-mass companion within the gap of the transition disk around pds 70. *Astronomy amp; Astrophysics*, 617:A44.

[Kutra et al., 2024] Kutra, T., Wu, Y., and Lithwick, Y. (2024). Irradiated disks may settle into staircases.

[Lesur and Papaloizou, 2009] Lesur, G. and Papaloizou, J. C. B. (2009). On the stability of elliptical vortices in accretion discs. *Astronomy amp; Astrophysics*, 498(1):1–12.

[Li et al., 2000] Li, H., Finn, J. M., Lovelace, R. V. E., and Colgate, S. A. (2000). Rossby Wave Instability of Thin Accretion Disks. II. Detailed Linear Theory. , 533(2):1023–1034.

[Li and Li, 2015] Li, S. and Li, H. (2015). Long-Time Sustainability of Rossby Wave Instability in Protoplanetary Disks with Dead Zone. In Pogorelov, N. V., Audit, E., and Zank, G. P., editors, *Numerical Modeling of Space Plasma Flows ASTRONUM-2014*, volume 498 of *Astronomical Society of the Pacific Conference Series*, page 102.

[Lin and Papaloizou, 1986] Lin, D. N. C. and Papaloizou, J. (1986). On the Tidal Interaction between Protoplanets and the Protoplanetary Disk. III. Orbital Migration of Protoplanets. , 309:846.

[Lin and Pierens, 2018] Lin, M.-K. and Pierens, A. (2018). Vortex survival in 3d self-gravitating accretion discs. *Monthly Notices of the Royal Astronomical Society*, 478(1):575–591.

[Long et al., 2018] Long , F. Pinilla, P., Herczeg , G. J. Harsono, D., Dipierro, G., Pascucci, I., Hendler, N., Tazzari, M., Ragusa, E., Salyk, C., Edwards, S., Lodato, G., van de Plas, G., Johnstone, D., Liu, Y., Boehler, Y., Cabrit, S., Manara, C. F., Menard, F., Mulders, G. D., Nisini, B., Fischer, W. J., Rigliaco, E., Banzatti, A., Avenhaus, H., and Gully-Santiago, M. (2018). Gaps and rings in an alma survey of disks in the taurus star-forming region. *The Astrophysical Journal*, 869(1):17.

[Lovelace and Hohlfeld, 1978] Lovelace, R. V. E. and Hohlfeld, R. G. (1978). Negative mass instability of flat galaxies. , 221:51–61.

[Lovelace and Hohlfeld, 2012] Lovelace, R. V. E. and Hohlfeld, R. G. (2012). Rossby wave instability with self-gravity. *Monthly Notices of the Royal Astronomical Society*, 429(1):529–533.

[Lovelace et al., 1999] Lovelace, R. V. E., Li, H., Colgate, S. A., and Nelson, A. F. (1999). Rossby Wave Instability of Keplerian Accretion Disks. , 513(2):805–810.

[Masset, 2000] Masset, F. (2000). FARGO: A fast eulerian transport algorithm for differentially rotating disks. , 141:165–173.

[Meheut et al., 2012] Meheut, H., Yu, C., and Lai, D. (2012). Rossby wave instability in 3D discs. , 422(3):2399–2406.

[Miranda et al., 2017] Miranda, R., Li, H., Li, S., and Jin, S. (2017). Long-lived dust asymmetries at dead zone edges in protoplanetary disks. *The Astrophysical Journal*, 835(2):118.

[Miranda and Rafikov, 2019] Miranda, R. and Rafikov, R. R. (2019). On the planetary interpretation of multiple gaps and rings in protoplanetary disks seen by alma. *The Astrophysical Journal Letters*, 878(1):L9.

[Miranda and Rafikov, 2020] Miranda, R. and Rafikov, R. R. (2020). Planet–disk interaction in disks with cooling: Basic theory. *The Astrophysical Journal*, 892(1):65.

[Muto et al., 2012] Muto, T., Grady, C. A., Hashimoto, J., Fukagawa, M., Hornbeck, J. B., Sitko, M., Russell, R., Werren, C., Curé, M., Currie, T., Ohashi, N., Okamoto, Y., Momose, M., Honda, M., Inutsuka, S., Takeuchi, T., Dong, R., Abe, L., Brandner, W., Brandt, T., Carson, J., Egner, S., Feldt, M., Fukue, T., Goto, M., Guyon, O., Hayano, Y., Hayashi, M., Hayashi, S., Henning, T., Hodapp, K. W., Ishii, M., Iye, M., Janson, M., Kandori, R., Knapp, G. R., Kudo, T., Kusakabe, N., Kuzuhara, M., Matsuo, T., Mayama, S., McElwain, M. W., Miyama, S., Morino, J.-I., Moro-Martin, A., Nishimura, T., Pyo, T.-S., Serabyn, E., Suto, H., Suzuki, R., Takami, M., Takato, N., Terada, H., Thalmann, C., Tomono, D., Turner, E. L., Watanabe, M., Wisniewski, J. P., Yamada, T., Takami, H., Usuda, T., and Tamura, M. (2012). Discovery of small-scale spiral structures in the disk of sao 206462 (hd 135344b): Implications for the physical state of the disk from spiral density wave theory. *The Astrophysical Journal*, 748(2):L22.

[Ono et al., 2016] Ono, T., Muto, T., Takeuchi, T., and Nomura, H. (2016). Parametric study of the rossby wave instability in a two-dimensional barotropic disk. *The Astrophysical Journal*, 823(2):84.

[Ono et al., 2018] Ono, T., Muto, T., Tomida, K., and Zhu, Z. (2018). Parametric study of the rossby wave instability in a two-dimensional barotropic disk. ii. nonlinear calculations. *The Astrophysical Journal*, 864(1):70.

[Paardekooper et al., 2010] Paardekooper, S.-J., Lesur, G., and Papaloizou, J. C. B. (2010). Vortex migration in protoplanetary disks. *The Astrophysical Journal*, 725(1):146–158.

[Pardo et al., 2001] Pardo, J. R., Cernicharo, J., and Serabyn, E. (2001). Atmospheric transmission at microwaves (ATM): an improved model for millimeter/submillimeter applications. *IEEE Transactions on Antennas and Propagation*, 49(12):1683–1694.

[Pérez et al., 2018] Pérez, L. M., Benisty, M., Andrews, S. M., Isella, A., Dullemond, C. P., Huang, J., Kurtovic, N. T., Guzmán, V. V., Zhu, Z., Birnstiel, T., Zhang, S., Carpenter, J. M., Wilner, D. J., Ricci, L., Bai, X.-N., Weaver, E., and Öberg, K. I. (2018). The Disk Substructures at High Angular Resolution Project (DSHARP). X. Multiple Rings, a Misaligned Inner Disk, and a Bright Arc in the Disk around the T Tauri star HD 143006. , 869(2):L50.

[Pierens and Lin, 2018] Pierens, A. and Lin, M.-K. (2018). On the evolution of vortices in massive protoplanetary discs. *Monthly Notices of the Royal Astronomical Society*.

[Rafikov, 2006] Rafikov, R. R. (2006). Atmospheres of Protoplanetary Cores: Critical Mass for Nucleated Instability. , 648(1):666–682.

[Regály et al., 2011] Regály, Z., Juhász, A., Sándor, Z., and Dullemond, C. P. (2011). Possible planet-forming regions on submillimetre images: Planet formation on submillimetre images. *Monthly Notices of the Royal Astronomical Society*, 419(2):1701–1712.

[Richard et al., 2013] Richard, S., Barge, P., and Le Dizès, S. (2013). Structure, stability, and evolution of 3D Rossby vortices in protoplanetary disks. , 559:A30.

[Segura-Cox et al., 2020] Segura-Cox, D. M., Schmiedeke, A., Pineda, J. E., Stephens, I. W., Fernández-López, M., Looney, L. W., Caselli, P., Li, Z.-Y., Mundy, L. G., Kwon, W., and Harris, R. J. (2020). Four annular structures in a protostellar disk less than 500,000 years old. *Nature*, 586(7828):228–231.

[Shakura and Sunyaev, 1973] Shakura, N. I. and Sunyaev, R. A. (1973). Black holes in binary systems. Observational appearance. , 24:337–355.

[Stone and Gardiner, 2010] Stone, J. M. and Gardiner, T. A. (2010). Implementation of the Shearing Box Approximation in Athena. , 189(1):142–155.

[Stone et al., 2020] Stone, J. M., Tomida, K., White, C. J., and Felker, K. G. (2020). The athena adaptive mesh refinement framework: Design and magnetohydrodynamic solvers. *The Astrophysical Journal Supplement Series*, 249(1):4.

[Suriano et al., 2018] Suriano, S. S., Li, Z.-Y., Krasnopolsky, R., and Shang, H. (2018). The formation of rings and gaps in magnetically coupled disc-wind systems: ambipolar diffusion and reconnection. *Monthly Notices of the Royal Astronomical Society*, 477(1):1239–1257.

[Takahashi and Inutsuka, 2014] Takahashi, S. Z. and Inutsuka, S.-i. (2014). Two-component secular gravitational instability in a protoplanetary disk: A possible mechanism for creating ring-like structures. *The Astrophysical Journal*, 794(1):55.

[Takahashi and Muto, 2018] Takahashi, S. Z. and Muto, T. (2018). Structure formation in a young protoplanetary disk by a magnetic disk wind. *The Astrophysical Journal*, 865(2):102.

[Tarczay-Nehéz et al., 2021] Tarczay-Nehéz, D., Rozgonyi, K., and Regály, Z. (2021). On the evolution of vortex in locally isothermal self-gravitating discs: a parameter study. *Monthly Notices of the Royal Astronomical Society*, 511(4):6055–6074.

[The CASA Team et al., 2022] The CASA Team, Bean, B., Bhatnagar, S., Castro, S., Meyer, J. D., Emonts, B., Garcia, E., Garwood, R., Golap, K., Villalba, J. G., Harris, P., Hayashi, Y., Hoskins, J., Hsieh, M., Jagannathan, P., Kawasaki, W., Keimpema, A., Kettenis, M., Lopez, J., Marvil, J., Masters, J., McNichols, A., Mehringer, D., Miel, R., Moellenbrock, G., Montesino, F., Nakazato, T., Ott, J., Petry, D., Pokorny, M., Raba, R., Rau, U., Schiebel, D., Schweighart, N., Sekhar, S., Shimada, K., Small, D., Steeb, J.-W., Sugimoto, K., Suoranta, V., Tsutsumi, T., van Bemmel, I. M., Verkouter, M., Wells, A., Xiong, W., Szomoru, A., Griffith, M., Glendenning, B., and Kern, J. (2022). Casa, the common astronomy software applications for radio astronomy. *Publications of the Astronomical Society of the Pacific*, 134(1041):114501.

[van der Marel et al., 2020] van der Marel, N., Birnstiel, T., Garufi, A., Ragusa, E., Christiaens, V., Price, D. J., Sallum, S., Muley, D., Francis, L., and Dong, R. (2020). On the diversity of asymmetries in gapped protoplanetary disks. *The Astronomical Journal*, 161(1):33.

[van der Marel et al., 2016] van der Marel, N., Cazzoletti, P., Pinilla, P., and Garufi, A. (2016). Vortices and Spirals in the HD135344B Transition Disk. , 832(2):178.

[van der Marel et al., 2015] van der Marel, N., van Dishoeck, E. F., Bruderer, S., Andrews, S. M., Pontoppidan, K. M., Herczeg, G. J., van Kempen, T., and Miotello, A. (2015). Resolved gas cavities in transitional disks inferred from co isotopologs with alma. *Astronomy amp; Astrophysics*, 585:A58.

[Youdin and Lithwick, 2007] Youdin, A. N. and Lithwick, Y. (2007). Particle stirring in turbulent gas disks: Including orbital oscillations. *Icarus*, 192(2):588–604.

[Zhang et al., 2015] Zhang, K., Blake, G. A., and Bergin, E. A. (2015). Evidence of fast pebble growth near condensation fronts in the hl tau protoplanetary disk. *The Astrophysical Journal*, 806(1):L7.

[Zhang and Zhu, 2020] Zhang, S. and Zhu, Z. (2020). The effects of disc self-gravity and radiative cooling on the formation of gaps and spirals by young planets. *Monthly Notices of the Royal Astronomical Society*, 493(2):2287–2305.

[Zhu et al., 2016] Zhu, Z., Ju, W., and Stone, J. M. (2016). Shock-driven accretion in circumplanetary disks: Observables and satellite formation. *The Astrophysical Journal*, 832(2):193.

[Zhu et al., 2014] Zhu, Z., Stone, J. M., Rafikov, R. R., and Bai, X.-n. (2014). Particle Concentration at Planet-induced Gap Edges and Vortices. I. Inviscid Three-dimensional Hydro Disks. , 785(2):122.

Appendix A

Convergence Tests

The goal of our work is to ascertain whether a vortex can generate a gas gap and dust ring within a disk, and to determine the location of the dust ring in relation to the shape of the vortex. The height of the dust ring is related to the steepness of the pressure bump at the outer edge of the gas gap, while the location of the dust ring is dictated by the shock location of the density waves, as indicated by the vortensity peaks. Consequently, achieving convergence in both the location of the vortensity peaks and the gas density profile is essential.

Figure A.1 illustrates the radial profiles of vortensity and gas density (right) for the 'A4' model at various resolutions: 64, 128, 256, and 512 cells/h for shearing box simulation. We find that the location of the vortensity peaks and the density profile converged at approximately 256 cells/h. Consequently, we selected 256 cells/h as the adequate resolution for our simulation and analysis.

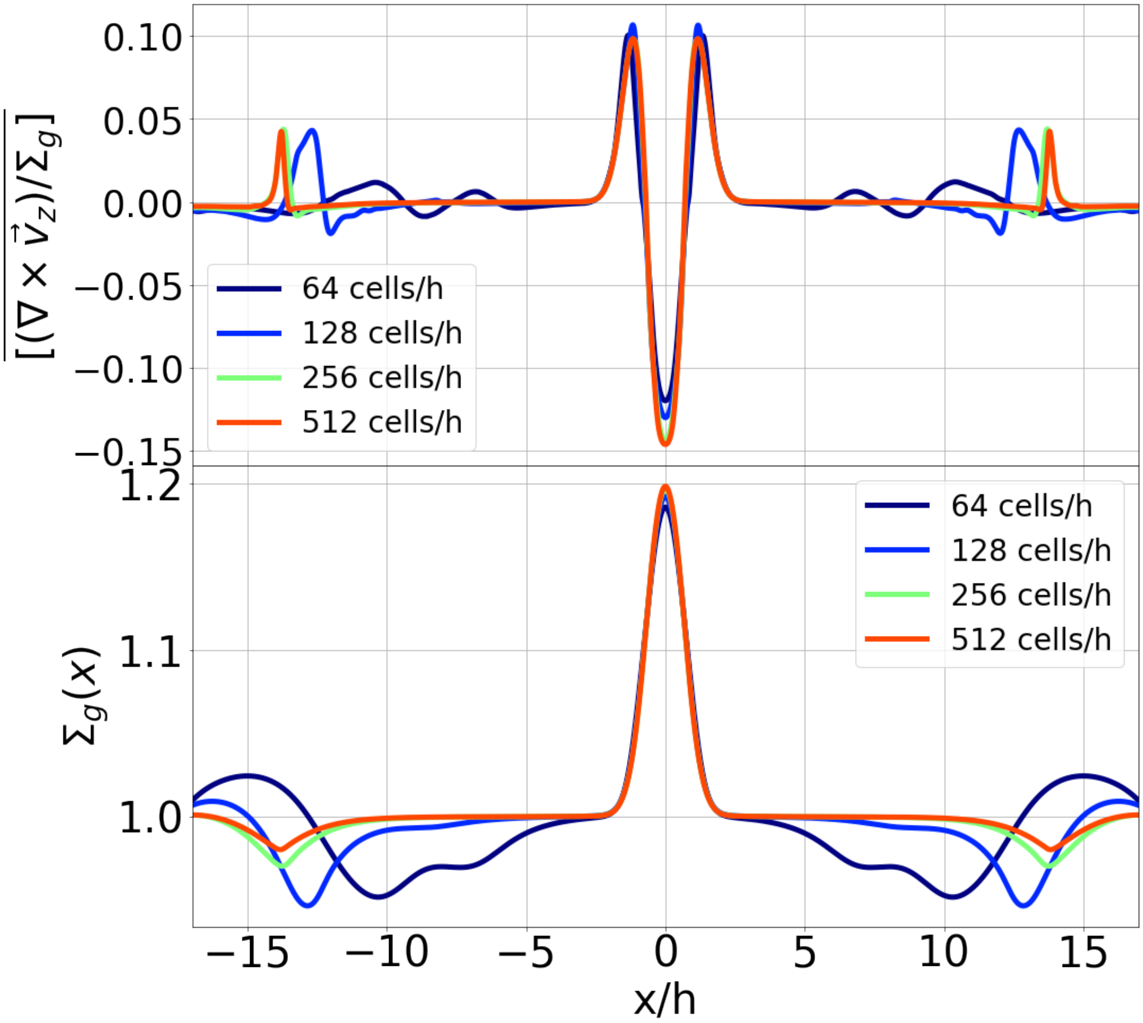

Figure A.1: Vortensity radial profile (top) and gas density radial profile (bottom) for the 'A4' model at different resolutions as 64, 128, 256 and 512 cells/h for shearing box simulation.